Title

Assembly of neuron- and radial glial cell-derived extracellular matrix molecules promotes radial migration of developing cortical neurons

Author names

Ayumu Mubuchi[1], Mina Takechi[2], Shunsuke Nishio[3], Tsukasa Matsuda[3], Yoshifumi Itoh[4], Chihiro Sato[2,5,6], Ken Kitajima[2,5,6], Hiroshi Kitagawa[7], Shinji Miyata[1,*]

Affiliations

[1] Graduate School of Agriculture, Tokyo University of Agriculture and Technology, Fuchu, Japan
[2] Graduate School of Bioagricultural Sciences, Nagoya University, Nagoya, Japan
[3] Faculty of Food and Agricultural Sciences, Fukushima University, Fukushima, Japan
[4] Kennedy Institute of Rheumatology, University of Oxford, Oxford, UK.
[5] Bioscience and Biotechnology Center, Nagoya University, Nagoya, Japan
[6] Institute for Glyco-core Research, Nagoya University, Nagoya, Japan
[7] Laboratory of Biochemistry, Kobe Pharmaceutical University, Kobe, Japan
*Correspondence: smiyata@go.tuat.ac.jp

Abstract

Radial neuronal migration is a key neurodevelopmental event for proper cortical laminar organization. The multipolar-to-bipolar transition, a critical step in establishing neuronal polarity during radial migration, occurs in the subplate/intermediate zone (SP/IZ), a distinct region of the embryonic cerebral cortex. It has been known that the extracellular matrix (ECM) molecules are enriched in the SP/IZ. However, the molecular constitution and functions of the ECM formed in this region remain poorly understood. Here, we identified neurocan (NCAN) as a major chondroitin sulfate proteoglycan in the SP/IZ. NCAN binds to both radial glial cell-derived tenascin-C (TNC) and hyaluronan (HA), a large linear polysaccharide, forming a ternary complex of NCAN, TNC, and HA in the SP/IZ. Developing cortical neurons make contact with the ternary complex during migration. The enzymatic or genetic disruption of the ternary complex impairs radial migration by suppressing the multipolar-to-bipolar transition. Furthermore, both TNC and NCAN promoted the morphological maturation of cortical neurons *in vitro*. The present results provide evidence for the cooperative role of neuron- and radial glial cell-derived ECM molecules in cortical development.

Keywords

Extracellular matrix; Cortical development; Radial migration; Proteoglycans; Hyaluronan; Tenascin

Introduction

The six-layered laminar structure of the mammalian cerebral cortex is achieved via the coordinated radial migration of neurons from their place of birth in the ventricular zone (VZ) to their final destination in the cortical plate (CP) (Barnes and Polleux, 2009; Taverna et al., 2014). Radial glial cells residing in the VZ are embryonic neural stem cells and a major source of neurons (Kriegstein and Alvarez-Buylla, 2009). During the neurogenesis period (from embryonic day (E) 12 to E18 in mice), radial glial cells divide asymmetrically to give rise to one self-renewing radial glial cell and one intermediate progenitor cell. Intermediate progenitor cells detach from the apical surface, lose their polarity, and further divide symmetrically to produce a pair of neurons above the VZ (Noctor et al., 2004). Newly born immature neurons transiently exhibit multipolar shapes with multiple neurites and move in random directions (Noctor et al., 2004; Tabata and Nakajima, 2003). Neurons then change their shape from multipolar to bipolar, extending leading and trailing processes in the subplate/intermediate zone (SP/IZ) (Hatanaka and Yamauchi, 2013; Jossin and Cooper, 2011; Namba et al., 2014; Ohtaka-Maruyama et al., 2018). Bipolar neurons attach to the radial fibers elongated from radial glial cells and migrate radially along these fibers toward their final destination in the CP. The leading and trailing processes of bipolar neurons eventually become the apical dendrite and axon. Therefore, radial glial cells play important dual roles in both producing neurons and guiding them to their proper locations.

The multipolar-to-bipolar transition is a critical step in establishing neuronal polarity. The intrinsic mechanisms underlying neuronal polarity have been investigated for a long time using primary cultured neurons *in vitro,* and the importance of cytoskeletal molecules, signaling cascades, and transcription factors has been demonstrated (Jossin, 2020; Namba et al., 2015). Polarity formation *in vivo* may differ from that *in vitro* because it occurs in a complex three-dimensional environment generated by the extracellular matrix (ECM), secreted factors, and neighboring cells. The ECM provides structural support to guarantee tissue integrity and regulates neuronal differentiation, maturation, and synaptic function in the brain (Barros et al., 2011; Faissner and Reinhard, 2015; Franco and Müller, 2011). The brain ECM is characterized by a predominance of chondroitin sulfate proteoglycans (CSPGs) (Fawcett et al., 2022; Maeda et al., 2011; Miyata and Kitagawa, 2017; Reinhard et al., 2016; Zimmermann and Dours-Zimmermann, 2008). It has long been known that CSPGs are enriched in the SP/IZ (Fukuda et al., 1997; Hoerder-Suabedissen and Molnár, 2015; Miller et al., 1995). Notably, the multipolar-to-bipolar transition occurs in the SP/IZ, a cell-sparse area rich in CSPGs. However, the molecular constitution and functions of the ECM formed in this region remain poorly understood.

CSPGs expressed in the brain, including neurocan (NCAN), aggrecan (ACAN), versican, and brevican, exhibit shared structural domains (Yamaguchi, 2000). The N-terminal domain interacts with hyaluronan (HA), a large linear polysaccharide chain that reaches several million Da in size (Day and Prestwich, 2002). The central region shows an extended structure and contains covalently bound chondroitin sulfate chains (Zimmermann and Dours-Zimmermann, 2008). Previous studies have demonstrated the critical roles of chondroitin sulfate chains in neural stem/progenitor cell proliferation and neuronal migration (Ishii and Maeda, 2008; Sirko et al., 2007; von Holst et al., 2006). The C-terminal domain of CSPGs binds to

tenascins, a group of multimeric glycoproteins (Aspberg et al., 1997; Yamaguchi, 2000). Many studies have reported that tenascin-C (TNC) expressed by radial glial cells in the embryonic brain plays a crucial role in controlling cell proliferation and differentiation in the VZ (see reviews by (Faissner et al., 2017; Faissner and Reinhard, 2015). While the involvement of TNC in the stem cell niche is well-established, its role in neuronal migration remains relatively unexplored. For instance, a previous study has demonstrated that anti-TNC antibodies inhibit the migration of cerebellar granule cells in explant cultures (Husmann et al., 1992).

We previously reported that HA accumulated in the SP/IZ of the developing mouse cerebral cortex (Takechi et al., 2020). Pharmacological inhibition of HA synthesis suppressed neurite outgrowth in cultured neurons *in vitro*. Nevertheless, the interplay between HA, CSPGs, and tenascins within a common pathway to regulate embryonic cortical development remains uncertain. In the present study, we aimed to investigate whether CSPGs, HA, and tenascins form a complex in the developing cerebral cortex and, if so, to determine the potential significance of this complex in neuronal migration and the multipolar-to-bipolar transition *in vivo*. We demonstrated that NCAN, a major CSPG produced by developing cortical neurons, is bound to HA in the SP/IZ *in vivo*. NCAN also interacted with radial glial cell-derived TNC, forming a ternary complex of HA, NCAN, and TNC. Developing cortical neurons made contact with the ternary complex during migration. The enzymatic or genetic disruption of the ternary complex retarded radial migration by suppressing the multipolar-to-bipolar transition. The present results provide evidence for the cooperative role of neuron- and radial glial cell-derived ECM molecules in cortical development.

Results

NCAN is a major CSPG produced by developing cortical neurons.

We attempted to identify the core proteins of CSPGs in the developing mouse brain using an antibody recognizing the neoepitope generated at the non-reducing terminus of chondroitin sulfate chains after digestion with chondroitinase ABC (Figure 1a) (Caterson, 2012). Immunoblot analysis of the mouse cerebral cortex at E18 indicated that a band at 130 kDa represented a major CSPG detected by the anti-neo epitope antibody (Figure 1b). However, the developing mouse cerebral cortex contained other minor CSPGs. The lack of staining from the undigested cerebral cortex confirmed the specificity of the antibody. In-gel tryptic digestion followed by a MALDI-TOF/TOF analysis identified the 130-kDa CSPG as an N-terminal portion NCAN (Figure 1c). Full-length >250-kDa NCAN is reportedly cleaved to generate the N-terminal 130-kDa fragment and C-terminal 150-kDa fragment (Figure 1d) (Rauch et al., 1992). Using an antibody to the N-terminal portion of NCAN, we found that the full-length and the N-terminal fragment of NCAN were both detected in the developing cerebral cortex (Figure 1e, f). In contrast, only the cleaved fragment was detected in the adult cerebral cortex, indicating the developmental stage-dependent proteolytic processing of NCAN (Figure 1e, f). Quantitative RT-PCR analysis showed high expression levels of *Ncan* during the late embryonic and early postnatal stages (Figure 1g).

We examined whether developing cortical neurons produce NCAN by immunoblot analysis of primary cultured cortical neurons. The full-length and the N-terminal fragment of NCAN were gradually

secreted into the culture medium (Figure 1h). To investigate the expression of *Ncan* mRNA during radial migration *in vivo*, we labeled radial glial cells in the VZ with GFP through *in utero* electroporation at E14 (Figure 1i, Figure 1-figure supplement 1). Quantitative RT-PCR analysis of GFP-positive cells isolated 0.6, 1, 2, and 4 days after labeling demonstrated that *Ncan* mRNA expression increased two days after labeling and was thereafter maintained (Figure 1j). These results indicated that developing cortical neurons themselves express *Ncan* mRNA and are capable of secreting NCAN.

NCAN forms a pericellular matrix with HA around developing neurons.

We investigated the distribution of *Ncan* mRNA in the developing cerebral cortex by *in situ* hybridization analysis. The widespread distribution of *Ncan* mRNA throughout the cerebral cortex indicated that NCAN production involves developing neurons as well as other cell populations, including radial glial cells (Figure 2a). In contrast to *Ncan* mRNA, NCAN protein densely accumulated in cell-sparse zones, such as the SP/IZ and marginal zone (MZ), but was less abundant in cell-dense regions, such as the CP and VZ (Figure 2b). This discrepancy in the *Ncan* mRNA and NCAN protein distribution pattern suggested a mechanism through which secreted NCAN protein localizes to the SP/IZ and MZ.

We noticed that the localization pattern of NCAN was similar to that of HA, which we previously reported (Figure 2c) (Takechi et al., 2020). Furthermore, NCAN and HA co-localized in cortical neuronal cultures as punctate signals at adhesion sites between the neuron and culture substrate, indicating that NCAN formed a pericellular matrix with HA (Figure 2d). To directly examine the binding between NCAN and HA, we pulled down endogenous HA and its interacting proteins using a biotinylated HA-binding protein (b-HABP), followed by immunoblotting with the antibody to the N-terminal portion of NCAN (Figure 2e). This analysis confirmed the interaction between NCAN and endogenous HA (Figure 2f). NCAN did not precipitate without b-HABP. The precipitation of NCAN depended on intact HA because NCAN disappeared from precipitates by digestion with hyaluronidase from *Streptomyces hyalurolyticus*, which specifically degrades HA and does not act on other glycosaminoglycans (Ohya and Kaneko, 1970). In addition, exogenously added biotinylated HA (b-HA) is also bound to the N-terminal portion of NCAN (Figure 2g). To verify the association between NCAN and HA by reciprocal co-immunoprecipitation, we recombinantly expressed the full-length, N- and C-terminal halves of NCAN fused with GFP (Figure 2-figure supplement 1a). After incubating with HA, we pulled down GFP-fused NCAN with anti-GFP nanobody-conjugated resin. Quantification of HA by ELISA demonstrated that the full-length and N-terminal half of NCAN precipitated a larger amount of HA than the C-terminal half (Figure 2-figure supplement 1b), supporting the binding between the N-terminal portion of NCAN and HA.

Radial glial cell-derived TNC interacts with the C-terminal portion of NCAN.

To further screen the interacting partners of NCAN, we pulled down proteins in the embryonic mouse brain lysate with GFP-fused full-length NCAN immobilized to resin (Figure 3a). LC-MS/MS analysis following trypsin digestion identified several proteins, including NCAN itself (Table 1). Among the identified

147 proteins, only TNC exhibited specific binding to NCAN. In contrast, intracellular proteins such as tubulin
148 and actin were found to be non-specific proteins detected even from the negative control resin. Co-
149 immunoprecipitation followed by immunoblot analysis showed that the C-terminal half, but not the N-
150 terminal half of NCAN, is bound to TNC (Figure 3b). Interactions between NCAN and TNC were dependent
151 on a divalent cation but not on chondroitin sulfate chains on NCAN consistent with previous findings
152 (Aspberg et al., 1997; Rauch et al., 1997). The expression of TNC at mRNA and protein levels peaked during
153 late embryonic brain development, similar to the expression pattern of NCAN (Figure 3c-e). *In situ*
154 hybridization analysis indicated that in the developing cerebral cortex at E16, *Tnc* mRNA was confined to
155 the VZ where the cell bodies of radial glia cells reside (Figure 3f), consistent with previous findings (Faissner
156 et al., 2017; Garcion et al., 2004). While some astrocytes express TNC during gliogenesis (E18 or later), it
157 has been documented that radial glial cells are the primary source of TNC in earlier stages (Faissner et al.,
158 2017). However, TNC protein was not restricted to the VZ but was also observed in the SP/IZ and MZ,
159 similar to the localization of NCAN (Figure 3g).
160 To predict the structure of the NCAN-TNC complex, we performed AlphaFold2 multimer analysis
161 (Figure 4a, b, Figure 4-figure supplement 1a). In this modeled complex, a C-type lectin domain (CLD) of
162 NCAN interacts with the 4th and 5th fibronectin type-III domains (FNIII) of TNC, which is consistent with
163 a previously reported structure of aggrecan (ACAN) and tenascin-R (TNR) (Figure 4-figure supplement 1b)
164 (Lundell et al., 2004). Amino acid residues in the interface of NCAN-TNC and ACAN-TNR complex were
165 highly conserved (Figure 4c, d). An Asn residue (Asn1148 in mNCAN and Asn2022 in rACAN), which
166 interacts with Ca^{2+} ions, was also conserved. Sequence alignments of fourteen FNIII of TNC indicated that
167 the amino acid residues in FNIII-4 involved in the binding to NCAN are not well conserved among other
168 FNIII (Figure 4-figure supplement 1c). From these results, we proposed that NCAN, HA, and TNC
169 cooperatively assemble a supramolecular complex as follows: (1) NCAN derived from developing neurons
170 and radial glial cells binds to multiple sites on a long chain of HA via the N-terminal Link modules; (2) The
171 hexamer of TNC secreted from radial glial cells cross-links NCAN through the interaction between the FNIII-
172 4 domain of TNC and the CLD of NCAN (Figure 4e).
173
174 **HA, NCAN, and TNC form the ternary complex in the developing cerebral cortex.**
175 To investigate the formation of a ternary complex of HA, NCAN, and TNC *in vivo*, we analyzed
176 the localization of these molecules in the embryonic mouse cerebral cortex. HA, NCAN, and TNC were co-
177 localized in the upper part of the SP/IZ and MZ of the developing cerebral cortex at E17 (Figure 5a). High
178 magnification views showed the aggregate-like deposition of these molecules in the SP/IZ (Figure 5b). Co-
179 localization of these three molecules was rarely observed in the CP or VZ. To investigate whether the ternary
180 complex interacts with the neuronal surface *in vivo*, we labeled developing cortical neurons by transfecting
181 a plasmid expressing a membrane-bound form of GFP at E14. Three days after *in utero* electroporation, GFP-
182 positive neurons exhibited a bipolar morphology in the upper SP/IZ and CP (Figure 5c, d), as previously
183 reported (Tabata and Nakajima, 2003). Z-stack projections of confocal images revealed that the ternary

complex frequently contacted the surface of migrating neurons (Figure 5c, d). Orthogonal views of 3D images showed the extracellular deposition of the ternary complex surrounding the cell body and neurites of bipolar neurons (Figure 5c, d).

Defects in NCAN and TNC retards neuronal migration.

To elucidate the role of the ternary complex during cortical development, we generated double knockout (DKO) mice for NCAN and TNC. Neither TNC nor NCAN was detected in the DKO mice, and the brain weights were not different compared to wild-type (WT) mice (Figure 6-figure supplement 1). Since the migratory patterns of neurons differ between the lateral and medial cortices, we took advantage of Flash Tag technology, in which an intraventricular injection of fluorescent dyes allows for the pulse labeling of progenitors in contact with the ventricle across the brain (Govindan et al., 2018; Telley et al., 2016; Yoshinaga et al., 2021). Radial glial cells in the M-phase were labeled at E14, and their progeny was analyzed two days later at E16. In the lateral cortex of WT mice, many labeled cells were migrating in the upper and lower SP/IZ, and a smaller population had already reached the CP (Figure 6a, b). In DKO mice, most cells resided beneath the lower SP/IZ, and very few reached the upper SP/IZ and CP. Bin analysis showed that DKO mice had a significantly lower percentage of labeled cells in the upper layers (Bin 1 and 2) and more cells in the lower layers (Bin 4 and 5) than WT mice (Figure 6b). In the medial cortex of WT mice, neurons reached the CP more quickly than in the lateral cortex (Figure 6c) (Yoshinaga et al., 2021). DKO mice exhibited slower neuronal migration in the medial cortex than WT mice, suggesting that the ternary complex facilitated the entry of neurons into the CP in a wide range of cortical regions.

Delayed migration in DKO mice was mostly restored after three days of labeling (Figure 6-figure supplement 2a, b). There was no difference in the number of cerebral cortical neurons between WT and DKO mice at 4 weeks of age (Figure 6-figure supplement 3a, b). No significant abnormalities were observed in the laminar structure in 4-week-old DKO mice. These results suggest that while the ternary complex is necessary for proper neuronal migration, some compensatory mechanisms may mitigate its effects in the postnatal brain. To assess whether the loss of NCAN and TNC affects stem cells/progenitors in the VZ, we compared the number of Pax6-positive radial glial cells and Tbr2-positive intermediate progenitor cells. Immunohistochemical analysis showed no significant differences between WT and DKO mice (Figure 6-figure supplement 4a). Additionally, the morphology of nestin-positive radial fibers was indistinguishable between WT and DKO mice (Figure 6-figure supplement 4b, c). These results suggested that the delay in neuronal migration was not due to the decreased proliferation of radial glial cells in DKO mice.

Single deletion of NCAN or TNC results in mild abnormalities in neuronal migration.

To investigate whether the loss of either NCAN or TNC alone would result in delayed neuronal migration similar to that observed in the DKO mice, we analyzed single KO mice lacking NCAN or TNC. In NCAN KO mice, a significantly lower percentage of labeled cells resided in the upper layer (Bin2), and more cells remained in the lower layer (Bin5) than in WT mice (Figure 7a). A similar trend was observed in

221 TNC KO mice, with a higher proportion of labeled cells in the lower layers than in WT mice (Figure 7a).
222 However, the delay in migration observed in the single KO mice was milder when compared to that observed
223 in DKO mice (Figure 6a-c). These results suggested that both NCAN and TNC are involved in neuronal
224 migration, but their combined deletion leads to a more pronounced impairment of neuronal migration.
225 We analyzed the effect of single deletion of NCAN or TNC on the ternary complex formation. In
226 WT mice, TNC was accumulated in the SP/IZ, whereas in NCAN KO mice, the localization of TNC shifted
227 to the lower layers (Figure 7b). Furthermore, TNC KO mice exhibited an attenuated accumulation of NCAN
228 in the SP/IZ compared with WT mice (Figure 7c). These results suggest that TNC and NCAN are mutually
229 required for their localization in the SP/IZ. Then, we examined whether the reduction in TNC accumulation
230 observed in NCAN KO mice can be rescued by forced expression of NCAN in migrating neurons. We
231 expressed Turbo-RFP alone or with GFP-fused full-length NCAN in NCAN KO brains by *in utero*
232 electroporation at E14 (Figure 7d). Immunostaining of TNC around the transfected Turbo-RFP-positive
233 neurons after two days indicated that expression of GFP-fused NCAN increased the accumulation of TNC
234 compared to controls (Figure 7e, f). Higher magnification views showed that TNC was localized adjacent to
235 GFP-fused NCAN (Figure 7g). Additionally, in DKO mice, the accumulation of HA, another component of
236 the ternary complex, was also decreased in the SP/IZ (Figure 7-figure supplement 1a). The reduction in HA
237 accumulation was less pronounced in single KO mice compared to DKO mice (Figure 7-figure supplement
238 1b), indicating that HA could not localize in the SP/IZ only when both NCAN and TNC were absent.
239
240 **Hyaluronidase digestion disrupts the ternary complex and inhibits neuronal migration.**
241 To further support the ternary complex formation *in vivo*, we degraded HA at E14 by
242 intraventricular injection of hyaluronidase. The majority of HA disappeared from the cerebral cortex two
243 days after the injection (Figure 8a). We noted that the staining intensity of NCAN and TNC significantly
244 decreased at the SP/IZ following the hyaluronidase treatment, indicating the interaction of these molecules
245 and the requirement of HA for the localization of NCAN and TNC. Immunoblot analysis showed that the
246 digestion of HA reduced the amount of NCAN and TNC in the cerebral cortex by approximately half,
247 confirming the essential role of HA in the retention of NCAN and TNC (Figure 8b, c). Migration assay using
248 Flash Tag showed that in comparisons with PBS-injected controls, a hyaluronidase injection at E14 inhibited
249 neuronal migration into the CP in the lateral and medial cortices (Figure 8d, e). However, the impact of
250 hyaluronidase treatment on neuronal migration was not as prominent as observed in DKO mice. This result
251 could be attributed to the fact that approximately half of NCAN and TNC remained in the tissue after
252 hyaluronidase digestion.
253
254 **DKO mice show delayed multipolar-to-bipolar transition during radial migration.**
255 To gain insights into the mechanisms underlying migration defects in DKO mice, we investigated
256 whether the loss of NCAN and TNC influenced the multipolar-to-bipolar transition. Fifty-three hours after
257 *in utero* electroporation with a cytosolic form of mCherry, we evaluated neuronal morphology based on the

following criteria: (1) the ratio of the length-to-width of labeled neurons as an indicator of cell shape; (2) the angle between major neurites and the ventricle surface; (3) the percentage of neurons with a bipolar morphology, defined as cells with a length-to-width ratio greater than three and an orientation angle greater than 70° (Figure 9a). *In utero* electroporation-mediated labeling also showed delayed neuronal migration in DKO mice, similar to Flask Tag labeling (Figure 9b). Morphological analysis revealed a significantly lower length-to-width ratio of neurons in DKO mice than in WT mice (Figure 9c, d). This result indicated that control neurons had an elongated shape, whereas neurons in DKO mice retained a rounded shape. Many neurons radially extended their major neurites towards the pia surface (between 70° and 90° relative to the ventricle surface) in WT mice, which is characteristic of bipolar neurons (Figure 9e). Compared with control neurons, the major neurites of DKO neurons were not directed toward the pia surface. Consistent with these results, we observed a significantly smaller proportion of bipolar neurons in DKO mice than in WT mice (Figure 9f). Therefore, retarded neuronal migration in DKO mice was associated with defects in the multipolar-to-bipolar transition.

Morphological maturation of cortical neurons by TNC and NCAN.

Next, we analyzed the effects of each component of the ternary complex on the morphological maturation of cortical neurons *in vitro*. We labeled progenitor cells with GFP at E14 by *in utero* electroporation and cultured dissociated neurons prepared at E15 on a glass plate coated with HA, NCAN, or TNC (Figure 10a). GFP-positive neurons on the control substrate, poly-L-ornithine (PLO), exhibited a typical morphological transition from stages 1 to 3 as follows (Figure 10b): Neurons initially have immature processes (stage 1) and then begin to extend multiple neurites of approximately equal lengths (stage 2); One of the neurites rapidly elongates to become the axon (stage 3), corresponding to the multipolar-to-bipolar transition *in vivo*. After two days of plating, culturing neurons on the TNC-coated plates significantly accelerated neurite outgrowth (Figure 10c). The length of the longest neurite notably increased when the glass plate was coated with 10 μg/mL of TNC (Figure 10d). In contrast, coating with 10 μg/mL of HA or NCAN did not significantly affect neurite elongation. Plating neurons on TNC also increased the total length and number of neurites (Figure 10e, f). This effect of TNC on neurite outgrowth was also evident after three days of plating (Figure 10-figure supplement 1a-d). The impact of TNC was further confirmed when the neurites of all neurons were stained with anti-Tuj-1 antibody instead of labeling a small population of neurons through *in utero* electroporation (Figure 10-figure supplement 2a-e). Closer observations found that TNC enhances the morphological transition of cortical neurons from stages 1 to 3 in a dose-dependent manner (Figure 10g), suggesting that TNC stimulates the multipolar-to-bipolar transition.

However, these findings did not rule out the potential involvement of NCAN and HA in the morphological transition since cortical neurons themselves are capable of secreting NCAN and HA in culture (Figure 1j, 2d). Indeed, in a previous study, we reported that pharmacological inhibition of HA synthesis led to the suppression of neurite outgrowth (Takechi et al., 2020). To further investigate the possible role of NCAN in neurite outgrowth, we cultured cortical neurons derived from WT and NCAN KO embryos (Figure

295 10h). After two and three days of plating, NCAN KO neurons exhibited a significantly suppressed elongation
296 of the longest neurite compared to WT neurons (Figure 10h, i, Figure 10-figure supplement 3a, b).
297 Additionally, the deletion of NCAN reduced the total length and number of neurites (Figure 10j, k, Figure
298 10-figure supplement 3c, d). These results indicated that TNC and NCAN play critical roles in the
299 morphological maturation of cortical neurons.
300
301 **Discussion**
302 The multipolar-to-bipolar transition of developing cortical neurons is essential for radial
303 migration and neuronal polarity. Defects in the multipolar-to-bipolar transition lead to neuronal
304 mispositioning, laminar structure disorganization, and cortical development malformation (Castello and
305 Gleeson, 2021; Fernández et al., 2016). Therefore, the timing and location of the multipolar-to-bipolar
306 transition need to be tightly controlled. The present results propose that the assembly of ECM molecules in
307 the SP/IZ provides an extracellular positional cue for migrating neurons that specify the site of the
308 multipolar-to-bipolar transition. Polarity formation *in vivo* occurs in a microenvironment or niche created in
309 the SP/IZ. A previous study found that pre-existing efferent axon tracts in the SP/IZ interacted with
310 migrating multipolar neurons to promote the formation of axons (Namba et al., 2014). Secreted soluble
311 factors also play significant roles in this process. A gradient of semaphorin 3A in the developing cerebral
312 cortex regulates neuronal migration and polarity by attracting apical dendrites and repulsing axons (Chen et
313 al., 2008; Polleux et al., 2000). Transforming growth factor-β initiates signaling pathways that specify
314 axons (Yi et al., 2010). Reelin, a glycoprotein secreted by Cajal-Retzius cells in the MZ, is essential for
315 completing neuronal migration and cortical lamination (D'Arcangelo et al., 1995; Jossin and Cooper,
316 2011). Therefore, a combination of ECM molecules, secreted factors, and neighboring cells regulates
317 neuronal polarity during cortical development.
318 Radial glial cells play a dual function during development: producing neurons and serving as
319 scaffolds for neuronal migration. The present study discovered another role for radial glial cells: they secrete
320 and deposit TNC to stimulate the morphological transition of migrating neurons in the SP/IZ. In
321 gyrencephalic species, such as humans, basal/outer radial glial cells residing in the outer sub-VZ generate
322 the majority of cortical neurons and are responsible for the expansion of the cerebral cortex (Kriegstein and
323 Alvarez-Buylla, 2009; Taverna et al., 2014). Basal/outer radial glial cells are characterized by the high gene
324 expression of several ECM molecules, including TNC (Fietz et al., 2012; Pollen et al., 2015), indicating that
325 basal/outer radial glial cells create a microenvironment that promotes neuronal migration. In addition, HA-
326 based ECM affects the cortical folding of the developing human neocortex (Long et al., 2018), suggesting
327 that the evolutionarily conserved ECM structure contributes to neocortex expansion in gyrencephalic species.
328 The tenascin gene family in vertebrates comprises four closely related members. They share
329 structural motifs: a cysteine-rich region at the N-terminus followed by EGF-like repeats, FNIIIs, and a
330 fibrinogen-like globe at the C-terminus. TNC monomers assemble into hexamers at the N-terminal region.
331 Distinct domains of TNC are involved in cell adhesion, cell repulsion, and neurite outgrowth promotion

332 (Andrews et al., 2009; Faissner et al., 2017; Götz et al., 1997; Lochter et al., 1991; Tucker and Chiquet-
333 Ehrismann, 2015). For example, alternatively spliced FNIIIs stimulate neurite outgrowth by binding to
334 neuronal surface contactin-1 in primary cultured neurons (Rigato et al., 2002). Several integrins have been
335 identified as receptors for TNC, and through this interaction, TNC influences cell adhesion, migration, and
336 proliferation (Tucker and Chiquet-Ehrismann, 2015). However, the mechanisms by which TNC secreted
337 from radial glial cells are presented to neurons *in vivo* remain unclear. Our analysis revealed that binding to
338 HA via NCAN was required for the deposition of TNC in the SP/IZ. Further studies are needed to identify
339 receptors for TNC on migrating neurons and its downstream signaling pathway that transmits information
340 from the extracellular environment to the inside of the cell.

341 There is a transition from embryonic- to adult-type ECM during brain development (Miyata et al.,
342 2012; Zimmermann and Dours-Zimmermann, 2008). The expression of NCAN and TNC is high in the
343 embryonic brain, whereas ACAN, brevican, and TNR increase during late postnatal development. In the adult
344 brain, ACAN cross-links HA and TNR and forms macromolecular aggregates around subpopulations of
345 neurons (Fawcett et al., 2022; Miyata and Kitagawa, 2017). This condensed ECM structure, called
346 perineuronal nets, is formed at the late postnatal stages and plays pivotal roles in neural plasticity, memory
347 consolidation, and circuit maturation (Fawcett et al., 2022). The ternary complex of ACAN, HA, and TNR
348 physically stabilizes existing synapses and inhibits new synapse formation. In perineuronal nets, high
349 molecular weight HA serves as a structural scaffold, facilitating the accumulation of ECM around
350 subpopulations of neurons in the adult brain. The present study showed that a structurally similar ternary
351 complex of NCAN, HA, and TNC was formed in the SP/IZ of the embryonic cortex but exerted distinct
352 functions in cortical development. The enzymatic digestion of HA impedes the accumulation of NCAN and
353 TNC within the SP/IZ, supporting that HA functions as a scaffold for ECM in the developing brain.
354 Alternatively, HA may transmit extracellular signals to developing neurons through cell surface HA receptors
355 such as CD44 (Skupien et al., 2014). Although the interaction of NCAN with HA and TNC was previously
356 reported *in vitro*, the present results revealed the formation of the ternary complex *in vivo* for the first time.
357 Full-length NCAN is detected during early development but not in adulthood, indicating that the proteolytic
358 cleavage of NCAN affects the assembly of the ternary complex. Screening using peptide library mixtures
359 revealed that matrix metalloprotease-2 cleaved the central region of NCAN *in vitro* (Turk et al., 2001). The
360 temporal control of matrix metalloproteases may affect neuronal migration via the assembly and disassembly
361 of the ECM.

362 We observed that single deletion of NCAN leads to mild abnormalities in neuronal migration. The
363 loss of NCAN may interfere with TNC localization and thus delay neuronal migration. Alternatively, the
364 binding of NCAN to cell adhesion molecules on the neuronal surfaces may affect neurite outgrowth
365 (Friedlander et al., 1994; Rauch et al., 2001). Genome-wide association studies identified a genetic variation
366 in NCAN as a risk factor for bipolar disorder and schizophrenia. However, the relationship between the
367 delayed neuronal migration observed in NCAN KO mice and the onset of neuropsychiatric disorders remains
368 uncertain. In adult NCAN KO mice, there are no apparent deficits in brain anatomy, morphology, or

ultrastructure (Zhou et al., 2001), which is consistent with our results that the delay in neuronal migration in DKO mice is transient. A recent study reported that the C-terminal portion of NCAN promotes synapse formation during postnatal development, which may be more relevant to neuropsychiatric disorders (Irala et al., 2023). These findings suggest that NCAN has different functions in the embryonic and adult brain.

In conclusion, the present study revealed that the assembly of NCAN, HA, and TNC forms the microenvironment in the SP/IZ, in which the multipolar-to-bipolar transition occurs. We uncovered that enzymatic and genetic disruption of the ternary complex impairs radial migration by inhibiting the multipolar-to-bipolar transition. Our findings shed light on the collaborative role of ECM molecules derived from neurons and radial glial cells in cortical development.

Acknowledgments

This research was funded by the Ministry of Education, Culture, Sports, Science & Technology, Japan [grant number 15K21067, 18K06130, and 21H05681 to S.M.] and the LOTTE Foundation [grant name Lotte Shigemitsu Prize to S.M.]. The authors thank Takeshi Kawauchi for valuable discussion, Makoto Matsuyama for technical advice on i-Gonad, Hitoshi Mori for technical assistance in mass spectrometry, Hidekazu Takahashi for the launch of a computational system for protein structure prediction, and members of Smart-Core-Facility Promotion Organization of Tokyo University of Agriculture and Technology for technical assistance. pCAG-GFP and pCAG-mGFP (Addgene plasmid # 11150 and #14757) were a gift from Connie Cepko. We thank the RIKEN Bioresource Center for *Tnc*-deficient mice (RBRC00169).

Author contributions

A.M., M.T., and S.M. designed research and conducted experiments. S.N. and T.M. contributed to mass spectrometry and protein structure prediction. C.S., K.K., H.K., and S.M. contributed to the biochemical analysis of NCAN and HA. C.S., K.K., T.M., I.Y., H.K., and S.M. interpreted data. A.M., S.N., and S.M. wrote the draft, and all authors revised and approved the final manuscript.

Declaration of interests

The authors declare no competing interests.

Materials and Methods

Mice used in the present study

All animal experimental studies were conducted with the approval of the Committee on Animal Experiments of the Graduate School of Bioagricultural Sciences, Nagoya University, and Tokyo University of Agriculture and Technology. Pregnant ICR (RRID: MGI:5462094) and C57BL/6NCrSlc (RRID: MGI:5295404) mice were purchased from Japan SLC (Shizuoka, Japan). TNC KO mice on a C57BL/6NJcl background were obtained from the RIKEN Bioresource Center (BRC No. RBRC00169)(Nakao et al., 1998). NCAN KO mice were generated using CRISPR-Cas9-based improved genome editing via oviductal nucleic acids delivery (i-GONAD) (Gurumurthy et al., 2019; Ohtsuka et al., 2018). A guide RNA targeting the mouse *Ncan* loci (Mm.Cas9.NCAN.1.AA: 5'-ACCTTAGTCCACTTGATCCGAGG-3') was chosen from Predesigned Alt-R CRISPR-Cas9 guide RNA on the Integrated DNA Technologies (IDT) website (https://sg.idtdna.com). Synthetic crRNAs, tracrRNA, and Cas9 Nuclease V3 were purchased from IDT. Surgical procedures for i-GONAD were performed under deep anesthesia at approximately 3 pm on the day on which a vaginal plug was detected. A mixture of 30 μM crRNA/tracrRNA complex and 1 mg/mL Cas9 Nuclease V3 was prepared in PBS. Approximately 2.5 μL of the mixture was injected into the oviduct upstream of the ampulla using a glass micropipette. The oviduct was clasped with a paired electrode (CUY652P2.5X4, NEPA Gene). Square electric pulses (poring pulse: 50 V, 5-ms pulse, 50-ms pulse interval, 3 pulses, 10% decay, ± pulse orientation, and transfer pulse: 10 V, 50-ms pulse, 50-ms pulse interval, 3 pulses, 40% decay, ± pulse orientation) were passed using an electroporator (NEPA21, NEPA Gene). Offspring were genotyped by DNA sequencing to identify founder animals. After first mating with TNC KO mice, the F1 generation was sequenced and further crossed to TNC KO mice to obtain DKO mice.

Cell lines used in the present study

The HEK293 (RCB1637) and HEK293T (RCB2202) cell lines were obtained from the Riken Cell Bank (Tsukuba, Japan) and used for protein pull-down experiments.

Immunoblotting

Mouse brains were homogenized in PBS containing 1% Triton X-100 and protease inhibitor cocktail (Sigma) and incubated on ice for 30 min. After centrifugation at 15,000 × g at 4°C for 30 min, the protein concentrations of supernatants (brain lysates) were assessed using a BCA assay kit (Thermo). Regarding chondroitinase ABC digestion, the brain lysate (70 μg as protein) was digested with 5 milliunits of protease-free chondroitinase ABC (Sikagaku Corp) at 37°C for 1 h. Digested and undigested lysates were denatured with 2% sodium dodecyl sulfate (SDS) and 5% mercaptoethanol at 95°C for 5 min. Proteins were separated using 6 or 10% SDS-polyacrylamide gel electrophoresis (PAGE) and transferred to polyvinylidene difluoride membranes. After blocking with 2% skim milk in PBS containing 0.1% Tween-20 (PBST), the membranes were incubated with an antibody recognizing the neoepitope of CSPGs (mouse, 1:50000, Millipore), anti-NCAN (sheep, 1:3000, R&D), anti-glyceraldehyde 3-phosphate dehydrogenase (GAPDH) (mouse, 1:10000,

Wako), anti-TNC (rat, 1:3000, R&D), and anti-GFP (rabbit, 1:3000, MBL) at 4°C overnight. After washing, the membranes were incubated with appropriate horseradish peroxidase (HRP)-conjugated secondary antibodies (1:2500) at room temperature for 1 h. Signals were detected with Immobilon Western Chemiluminescent HRP Substrate (Millipore) and imaged on a LuminoGraph I (ATTO).

Histochemistry

Mouse embryos were transcardially perfused with PBS, followed by 4% paraformaldehyde in PBS. Brains were removed and post-fixed overnight with 4% paraformaldehyde in PBS. Coronal sections (thickness of 80 μm) were cut with the vibratome VT1200 (Leica). Sections were permeabilized with 0.25% Triton X-100 in PBS and then blocked with PBST containing 2% bovine serum albumin (Sigma). Sections were incubated at 4°C overnight with biotinylated HA-binding protein (b-HABP) (1:400, Hokudo), anti-NCAN (sheep, 1:400, R&D), anti-TNC (rat, 1:400, R&D), anti-Pax6 (rabbit, 1:400, Invitrogen), anti-Tbr2 (mouse, 1:400, Wako), anti-Nestin (mouse, 1:400, Millipore), anti-NeuN (rabbit, 1:1000, Proteintech), and Alexa Fluor 488-conjugated anti-GFP (rabbit, 1:1000, Invitrogen). After washing, sections were incubated with the appropriate Alexa Fluor conjugate secondary antibody and streptavidin (Thermo), followed by cell nuclear staining with DAPI (0.1 μg/mL). Images were captured with the AX R confocal microscope (Nikon) or LSM 710 NLO confocal microscope (Carl Zeiss). In a three-dimensional reconstruction, images were captured using the Z-stack function of the confocal microscope, and Z-projection and orthogonal views were obtained by ImageJ FIJI software.

Quantitative reverse transcription (RT)-PCR

Total RNA from the developing mouse cerebral cortex and isolated GFP-positive cells were prepared using the RNeasy mini kit (Qiagen). cDNA was synthesized using SuperScript III reverse transcriptase (Thermo). Real-time RT-PCR was performed with the PowerUp SYBR Green Master Mix (Thermo) in the StepOne PCR system (Thermo). All primers used are listed in the Key Resources table. Relative gene expression was calculated using the comparative cycle threshold (Ct) method. Expression levels were normalized to *Gapdh*.

***In situ* hybridization**

Target sequences detecting *Ncan* and *Tnc* were amplified from mouse brain cDNA and cloned into the pSPT 19 vector (Roche). All primers used for probe amplification are listed in the Key Resources table. Digoxigenin (DIG)-labeled sense and antisense probes were generated with T7 and Sp6 RNA polymerase using a DIG RNA labeling kit (Roche) according to the manufacturer's instructions. RNA probes were purified with the RNeasy Mini Kit (Qiagen) and quantified using a Nanodrop (Thermo Fisher Scientific). ICR mouse embryos were removed from pregnant females at E16 and perfused with 4% paraformaldehyde in PBS. Brains were post-fixed overnight with 4% paraformaldehyde in PBS and embedded in OCT compound (Sakura Finetek). Frozen sections were cut coronally with a Leica Jung CM3000 cryostat (Leica) at a thickness of 20 μm. Brain sections were fixed with 4% paraformaldehyde in PBS, treated with 1 μg/mL

472 proteinase K, permeabilized with 0.3% Triton X-100 in PBS, and hybridized with 0.5 μg/mL DIG-labeled
473 probes at 70°C overnight in a moist chamber. After washing three times with 0.2 × saline-sodium citrate at
474 70°C for 30 min, sections were blocked with 10% blocking reagent (Roche) at room temperature for 1 h and
475 incubated with alkaline phosphatase-conjugated anti-DIG antibody (Roche) overnight at 4°C. The
476 hybridization signal was developed with NBT/BCIP solution (Roche).
477
478 **Identification of the 130-kDa band by MALDI-TOF/TOF**
479 Ten E18 mouse brains were homogenized in 10 mL of Hanks' Balanced Salt Solution (Gibco) containing 1%
480 Triton X-100, 10 mM HEPES (pH 7.6) (Gibco), and protease inhibitor cocktail (Sigma) and incubated on ice
481 for 1 h. After centrifugation at 15,000 × g at 4°C for 30 min, the supernatant was applied to a DEAE-
482 Toyopearl 650 M column (1 mL, Tosoh) equilibrated with buffer A (0.1% Triton X-100, 10 mM Tris–HCl,
483 pH 7.5). The column was washed with buffer A containing 0.25 M NaCl and then eluted with buffer A
484 containing 0.5 M NaCl. The eluent was diluted with a four-fold volume of buffer A and digested with 50
485 milliunits of chondroitinase ABC (Sikagaku Corp) at 37°C for 4 h. The digest was again applied to a DEAE-
486 Toyopearl 650 M column (0.4 mL) and eluted with buffer A containing 0.25 M NaCl. The eluent was applied
487 to a heparin-agarose column (0.3 mL, Sigma), and the flow-through fraction was collected. After
488 ultrafiltration with the YM-10 membrane (Amicon), the concentrate was separated using 6% SDS-PAGE.
489 After staining with Coomassie Brilliant Blue, the 130-kDa band was cut out as a gel piece and digested with
490 trypsin (Promega) at 37°C overnight. The recovered tryptic peptides were subjected to nano-LC (DiNa Nano
491 LC system, KYA Technologies), and eluted fractions were spotted on the MALDI plate (AB SCIEX) with α-
492 cyano-4-hydroxyciccanic acid (Shimadzu) as a matrix using the Direct nano LC/MALDI Spotter (KYA
493 technologies). Peptides were analyzed for identification using a MALDI mass spectrometer (TOF/TOF 5800,
494 AB SCIEX). MS/MS data were analyzed using MASCOT software (Matrix Science) as previously described
495 (Sakurai et al., 2018).
496
497 **Precipitation of HA-binding molecules from mouse brain lysate** (Sugitani et al., 2021).
498 One hundred microliters of the E16 mouse brain lysate were digested with 1 unit of hyaluronidase from
499 *Streptomyces hyalurolyticus* (Sigma) at 37°C for 1 h. Digested and undigested samples were incubated with
500 1.25 μg of b-HABP (Hokudo) or 0.25 ng of biotinylated HA (b-HA) (PG research) at 4°C overnight, followed
501 by precipitation by mixing with 25 μL streptavidin-coupled magnetic beads (Thermo) at room temperature
502 for 1 h. After washing the precipitates with PBST, the supernatant, and precipitates were digested with 5
503 milliunits of chondroitinase ABC (Sikagaku Corp) at 37°C for 2 h, denatured by SDS at 95°C for 5 min, and
504 then analyzed by immunoblotting, as described above.
505
506 **Construction of GFP-fused NCAN-expressing plasmids**
507 We amplified the full-length *Ncan* sequence by PCR from the mouse brain cDNA library and assembled it
508 into the pCAG-GFP vector using the NEBuilder HiFi DNA Assembly Master Mix (New England Biolabs)

509 or In-Fusion HD Cloning Kit (TaKaRa). The GFP-fused full-length NCAN-expressing plasmid was
510 constructed by inserting the fragment encoding GFP amplified from the pCAG-GFP vector into the central
511 region of NCAN (corresponding to Val641 to Leu644). The plasmids expressing the N- and C-terminal halves
512 of NCAN were constructed by deleting the C-terminal and N-terminal regions from full-length NCAN using
513 the KOD-Plus Mutagenesis Kit (Toyobo).
514
515 **Immobilization of GFP-fused NCAN on agarose resin**
516 HEK293 or HEK293T cells were transfected with plasmids expressing GFP-fused NCAN using Lipofectamine
517 3000 (Thermo) or PEI Max (Polysciences). After three or four days, recombinant proteins were isolated from
518 the culture medium by incubating anti-GFP nanobody-conjugated agarose (Chromotek). In some experiments,
519 we quantified the amounts of GFP-fused full-length, N-terminal half, and C-terminal half of NCAN in the
520 culture medium by immunoblotting with anti-GFP antibody and used equal amounts of GFP-fused NCAN
521 for immobilization.
522
523 **Binding of HA and GFP-fused NCAN**
524 GFP fused-NCAN immobilized to agarose was incubated with 2 μg /ml of HA (600-1200 kDa, PG research)
525 in PBS at 4°C overnight. After washing with PBS, HA bound to agarose resin was released by denaturation
526 at 95°C for 10 min. HA concentrations were measured by enzyme-linked immunosorbent assays (ELISA),
527 as previously reported (Egorova et al., 2023). Briefly, each well of a 96-well plate (Iwaki) was coated with
528 0.1% HABP (Cosmo-bio) at 4°C overnight. After washing with PBST, each well was blocked with 1%
529 BLOCK ACE (KAC) in PBS at 37°C for 2 h, followed by incubation with 1 mg/mL HA (Wako) in the
530 blocking solution at 37°C for 1 h. After washing, a mixture of 0.05% b-HABP (Hokudo) and the cerebrum
531 lysates was added to each well and incubated at 37°C for 1 h. b-HABP was detected by HRP-conjugated
532 streptavidin (1:25000, Wako) and ELISA POD Substrate TMB (Nacalai Tesque).
533
534 **Identification of NCAN interactors by LC-MS/MS analysis**
535 GFP-fused NCAN was immobilized on anti-GFP nanobody-conjugated agarose resin. Resin without NCAN
536 was used as a negative control. NCAN-conjugated and unconjugated resins were incubated with embryonic
537 mouse brain lysates at 4°C overnight. After washing with PBST, precipitated proteins were denatured with 8
538 M urea, subjected to reductive alkylation by dithiothreitol and iodoacetamide, and then digestion by trypsin
539 (Promega). The resultant peptide fragments were analyzed using the LC-MS/MS system (QTRAP5500, AB
540 Sciex) as previously described (Sakurai et al., 2018). MS/MS data were compiled using Mascot Distiller
541 (Matrix Science) and analyzed with MASCOT software (Matrix Science). Data filtering limits were set at a
542 peptide probability ≥95% and a minimum peptide number of 3 per protein.
543
544 **Structure prediction using AlphaFold2**
545 Based on the previous rACAN-TNR complex structure (PDB ID 1TDQ) (Lundell et al., 2004), we selected

546 the amino acid sequences of the C-terminal part of mNCAN (T961-I1224) and FNIII-1-5 of mTNC (S624-
547 E1073). We generated five complex models using AlphaFold2 multimer (v2) (Evans et al., 2022)
548 implemented in ColabFold (Mirdita et al., 2022). ColabFold ran with default parameters. All structures are
549 visualized using PyMOL v.2.5.0 (Schrödinger, LLC).
550
551 **Sequence alignment**
552 Alignments were generated using MAFFT (Katoh and Standley, 2013) and visualized using ESPript3 (Robert
553 and Gouet, 2014). Amino acid residues involved in the interface region of the predicted mNCAN-TNC
554 complex were analyzed using PDBsum (Laskowski et al., 2018) or Protein Interactions Calculator (PIC)
555 webserver (Tina et al., 2007).
556
557 **Intraventricular injection of hyaluronidase**
558 Pregnant WT mice were anesthetized with isoflurane (3% for induction and 2% for maintenance) during the
559 surgery using an animal anesthetizer (Muromachi). Using a pulled glass capillary, we injected 1 to 2 μL of
560 hyaluronidase from *S. hyalurolyticus* (1 unit/μl, Sigma) or PBS into the lateral ventricle. Fast Green dye
561 (Wako) was co-injected to visualize successful injections with hyaluronidase. After injections, the uterine
562 horns were placed back into the abdominal cavity to allow further embryonic growth. Coronal sections
563 (thickness of 80 μm) were prepared 2 days after injections and analyzed histochemically to detect HA, NCAN,
564 and TNC as described above. Regarding staining intensity profiles, a 50-μm-wide area spanning the CP to
565 VZ was divided into 100 equal bins, and the fluorescence intensity of each region was assessed using ImageJ
566 FIJI.
567
568 **Neuronal migration analysis by Flash Tag (FT)**(Govindan et al., 2018; Yoshinaga et al., 2021)
569 We injected carboxyfluorescein diacetate succinimidyl ester (1 mM in PBS, Dojindo) into the lateral
570 ventricle at E14. After 2 or 3 days, coronal sections (thickness of 80 μm) were prepared, and fluorescent
571 images were captured as described above. The top 10% of cells with high fluorescence intensity were
572 extracted and analyzed using ImageJ FIJI. The cerebral cortex was divided into five equal areas (bins 1–5)
573 from the pia to the ventricle, and the proportion of FT-labeled cells in each bin was calculated. For the
574 experiments investigating the effects of hyaluronidase shown in Figure 8, we used WT littermate mice and
575 simultaneously injected 1 unit of hyaluronidase or PBS with the fluorescent dye. In the experiments
576 examining neuronal migration in WT, DKO, NCAN KO, and TNC KO mice shown in Figure 6, Figure 6-
577 figure supplement 2, and Figure 7, we analyzed embryos from different dams with four different genotypes.
578
579 ***In utero* electroporation**
580 Mouse embryos at E14 or E15 were electroporated *in utero* to label neural progenitor cells in the VZ, as
581 previously described (Tabata and Nakajima, 2003; Takechi et al., 2020). During surgery, pregnant mice
582 were initially anesthetized with isoflurane (3% for induction and 2% for maintenance) using an animal

583 anesthetizer (Muromachi). Using a pulled glass capillary, we injected 1 to 2 μL of plasmid solution (1
584 μg/μL) into the lateral ventricle. The head was clasped with a paired electrode (CUY650P5, NEPA Gene),
585 and square electric pulses (33 V for 50 ms, five times in 950-ms intervals) were passed using an
586 electroporator (NEPA21, NEPA Gene). After electroporation, the uterine horns were placed back into the
587 abdominal cavity to allow further embryonic growth.
588
589 **Forced expression of GFP-fused NCAN in NCAN KO mice**
590 NCAN KO embryos at E14 were electroporated *in utero* with pCAG-Turbo-RFP alone or with GFP-fused
591 full-length NCAN. Coronal sections (thickness of 80 μm) were prepared 2 days after electroporation and
592 analyzed histochemically to detect TNC and GFP-fused NCAN as described above. The staining intensity of
593 TNC around Turbo-RFP-positive neurons (59 × 59 μm area) was measured using ImageJ FIJI.
594
595 **Morphological analysis of cortical neurons**
596 Neural progenitor cells in the VZ were transfected with pCAG-mCherry by *in utero* electroporation at E14.
597 After 53 h, coronal sections (thickness of 80 μm) were prepared, and fluorescent images were captured as
598 described above. Using ImageJ FIJI, neuronal morphology was evaluated by measuring the length-to-width
599 ratio of labeled neurons and the angle between major neurites and the ventricle surface. Bipolar neurons were
600 defined as cells with a length-to-width ratio greater than three and an orientation angle greater than 70°. In
601 Figure 9, we analyzed embryos from different WT and DKO dams to compare neuronal morphology.
602
603 **Isolation of migrating neurons from the cerebral cortex**
604 GFP labeling followed by cell sorting was performed as previously reported (Takechi et al., 2020). Briefly,
605 neural progenitor cells in the VZ of the cerebral cortex at E14 were transfected with pCAG-GFP using *in*
606 *utero* electroporation as described above. Embryonic brains were harvested 0.6–4 days later, and GFP-
607 positive regions were dissected from the cerebral cortices under a fluorescence stereomicroscope (Leica).
608 Cortical fragments were incubated in 0.25% trypsin and mechanically dispersed by gentle pipetting to
609 dissociate single cells. GFP-positive cells were isolated from the single-cell suspension by sorting using a
610 JSAN fluorescence-activated cell sorter (Bay Bioscience).
611
612 **Primary cultured cortical neurons**
613 Cover glasses were pre-coated with 20 μg/mL poly-L-ornithine (PLO) (Wako) at 37°C overnight and then
614 overlaid with 0.1–10 μg/mL of recombinant human TNC (R&D), recombinant human NCAN (R&D), and
615 HA (600–1200 kDa, PG research) at 37°C for 3 h. WT and NCAN KO brains were harvested 24 h after *in*
616 *utero* electroporation with pCAG-GFP at E14 (Mubuchi et al., 2022). GFP-positive regions were dissected
617 from the cerebral cortices under a fluorescence stereomicroscope (Leica). Cortical fragments were incubated
618 in 20 units/mL papain (Worthington Biochemical Corporation) and mechanically dispersed by gentle
619 pipetting. Dissociated cells were plated on ECM-coated cover glasses at a density of 50,000 or 100,000 cells

per well (1.9 mm^2). Cells were maintained for 1 to 3 days in Neurobasal Plus Medium (Thermo) supplemented with 2% B-27 Plus (Thermo), 5% horse serum (Sigma), and antibiotics (Thermo). Cultures were fixed with 4% paraformaldehyde, stained with an Alexa 488-conjugated anti-GFP antibody (Thermo) and anti-Tuj-1 (mouse, 1:1000, Sigma), and imaged as described above. For GFP-labeled neurons, processes longer than 10 μm were measured as neurites and analyzed using NeuronJ (Meijering et al., 2004). For neurons stained with anti-Tuj-1 antibody, neurites were analyzed using AutoNeuriteJ (Boulan et al., 2020; Mubuchi et al., 2022). Neurons without neurites were classified as stage 1, neurons with neurites shorter than 50 μm as stage 2, and neurons with neurites longer than 50 μm as stage 3. Regarding immunoblotting in Figure 1h and immunostaining in Figure 2d, dissociated cells were plated on PLO-coated cover glasses at 200,000 and 50,000 cells per well, respectively.

Quantification and statistical analysis

All data are presented as the mean ± SD. Statistical analyses were performed using Python within the Jupyter Notebooks environment and Easy R (Kanda, 2013). An unpaired, two-tailed Student's t-test was used to compare results from two groups. Dunnett's test was used to compare multiple experimental groups against the control group. A p-value <0.05 was considered to be significant. Details of statistical analyses, including the statistical tests used, N values, and p values, may be found in the relevant figures and figure legends.

References

Andrews MR, Czvitkovich S, Dassie E, Vogelaar CF, Faissner A, Blits B, Gage FH, ffrench-Constant C, Fawcett JW. 2009. α9 Integrin Promotes Neurite Outgrowth on Tenascin-C and Enhances Sensory Axon Regeneration. *J Neurosci* 29:5546–5557. doi:10.1523/JNEUROSCI.0759-09.2009

Aspberg A, Miura R, Bourdoulous S, Shimonaka M, Heinegârd D, Schachner M, Ruoslahti E, Yamaguchi Y. 1997. The C-type lectin domains of lecticans, a family of aggregating chondroitin sulfate proteoglycans, bind tenascin-R by protein-protein interactions independent of carbohydrate moiety. *Proc Natl Acad Sci U S A* 94:10116–10121. doi:10.1073/pnas.94.19.10116

Barnes AP, Polleux F. 2009. Establishment of axon-dendrite polarity in developing neurons. *Annu Rev Neurosci* 32:347–381. doi:10.1146/annurev.neuro.31.060407.125536

Barros CS, Franco SJ, Müller U. 2011. Extracellular matrix: functions in the nervous system. *Cold Spring Harb Perspect Biol* 3:a005108. doi:10.1101/cshperspect.a005108

Boulan B, Beghin A, Ravanello C, Deloulme J-C, Gory-Fauré S, Andrieux A, Brocard J, Denarier E. 2020. AutoNeuriteJ: An ImageJ plugin for measurement and classification of neuritic extensions. *PLoS One* 15:e0234529. doi:10.1371/journal.pone.0234529

Castello MA, Gleeson JG. 2021. Insight into developmental mechanisms of global and focal migration disorders of cortical development. *Current Opinion in Neurobiology* 66:77–84. doi:10.1016/j.conb.2020.10.005

Caterson B. 2012. Fell-Muir Lecture: Chondroitin sulphate glycosaminoglycans: fun for some and confusion for others. *International Journal of Experimental Pathology* 93:1–10. doi:10.1111/j.1365-2613.2011.00807.x

Chen G, Sima J, Jin M, Wang K-Y, Xue X-J, Zheng W, Ding Y-Q, Yuan X-B. 2008. Semaphorin-3A guides radial migration of cortical neurons during development. *Nat Neurosci* 11:36–44. doi:10.1038/nn2018

D'Arcangelo G, Miao GG, Chen SC, Soares HD, Morgan JI, Curran T. 1995. A protein related to extracellular matrix proteins deleted in the mouse mutant reeler. *Nature* 374:719–723. doi:10.1038/374719a0

Day AJ, Prestwich GD. 2002. Hyaluronan-binding proteins: tying up the giant. *J Biol Chem* 277:4585–4588. doi:10.1074/jbc.R100036200

Egorova D, Nomura Y, Miyata S. 2023. Impact of hyaluronan size on localization and solubility of the extracellular matrix in the mouse brain. *Glycobiology* cwad022. doi:10.1093/glycob/cwad022

Evans R, O'Neill M, Pritzel A, Antropova N, Senior A, Green T, Žídek A, Bates R, Blackwell S, Yim J, Ronneberger O, Bodenstein S, Zielinski M, Bridgland A, Potapenko A, Cowie A, Tunyasuvunakool K, Jain R, Clancy E, Kohli P, Jumper J, Hassabis D. 2022. Protein complex prediction with AlphaFold-Multimer. doi:10.1101/2021.10.04.463034

Faissner A, Reinhard J. 2015. The extracellular matrix compartment of neural stem and glial progenitor cells. *Glia* 63:1330–1349. doi:10.1002/glia.22839

Faissner A, Roll L, Theocharidis U. 2017. Tenascin-C in the matrisome of neural stem and progenitor cells. *Molecular and Cellular Neuroscience* 81:22–31. doi:10.1016/j.mcn.2016.11.003

Fawcett JW, Fyhn M, Jendelova P, Kwok JCF, Ruzicka J, Sorg BA. 2022. The extracellular matrix and perineuronal nets in memory. *Mol Psychiatry*. doi:10.1038/s41380-022-01634-3

Fernández V, Llinares-Benadero C, Borrell V. 2016. Cerebral cortex expansion and folding: what have we learned? *EMBO J* 35:1021–1044. doi:10.15252/embj.201593701

Fietz SA, Lachmann R, Brandl H, Kircher M, Samusik N, Schröder R, Lakshmanaperumal N, Henry I, Vogt J, Riehn A, Distler W, Nitsch R, Enard W, Pääbo S, Huttner WB. 2012. Transcriptomes of germinal zones of human and mouse fetal neocortex suggest a role of extracellular matrix in progenitor self-renewal. *PNAS* 109:11836–11841. doi:10.1073/pnas.1209647109

Franco SJ, Müller U. 2011. Extracellular matrix functions during neuronal migration and lamination in the mammalian central nervous system. *Dev Neurobiol* 71:889–900. doi:10.1002/dneu.20946

Friedlander DR, Milev P, Karthikeyan L, Margolis RK, Margolis RU, Grumet M. 1994. The neuronal chondroitin sulfate proteoglycan neurocan binds to the neural cell adhesion molecules Ng-CAM/L1/NILE and N-CAM, and inhibits neuronal adhesion and neurite outgrowth. *J Cell Biol* 125:669–680. doi:10.1083/jcb.125.3.669

Fukuda T, Kawano H, Ohyama K, Li H-P, Takeda Y, Oohira A, Kawamura K. 1997. Immunohistochemical localization of neurocan and L1 in the formation of thalamocortical pathway of developing rats. *J Comp Neurol* 382:141–152. doi:10.1002/(SICI)1096-9861(19970602)382:2<141::AID-CNE1>3.0.CO;2-3

Garcion E, Halilagic A, Faissner A, ffrench-Constant C. 2004. Generation of an environmental niche for neural stem cell development bythe extracellular matrix molecule tenascin C. *Development* 131:3423–3432. doi:10.1242/dev.01202

Götz M, Bolz J, Joester A, Faissner A. 1997. Tenascin-C Synthesis and Influence on Axonal Growth During Rat Cortical Development. *European Journal of Neuroscience* 9:496–506. doi:10.1111/j.1460-9568.1997.tb01627.x

Govindan S, Oberst P, Jabaudon D. 2018. In vivo pulse labeling of isochronic cohorts of cells in the central nervous system using FlashTag. *Nat Protoc* 13:2297–2311. doi:10.1038/s41596-018-0038-1

Gurumurthy CB, Sato M, Nakamura A, Inui M, Kawano N, Islam MA, Ogiwara S, Takabayashi S, Matsuyama M, Nakagawa S, Miura H, Ohtsuka M. 2019. Creation of CRISPR-based germline-genome-engineered mice without ex vivo handling of zygotes by i-GONAD. *Nat Protoc* 14:2452–2482. doi:10.1038/s41596-019-0187-x

Hatanaka Y, Yamauchi K. 2013. Excitatory Cortical Neurons with Multipolar Shape Establish Neuronal Polarity by Forming a Tangentially Oriented Axon in the Intermediate Zone. *Cerebral Cortex* 23:105–113. doi:10.1093/cercor/bhr383

Hoerder-Suabedissen A, Molnár Z. 2015. Development, evolution and pathology of neocortical subplate neurons. *Nat Rev Neurosci* 16:133–146. doi:10.1038/nrn3915

Husmann K, Faissner A, Schachner M. 1992. Tenascin promotes cerebellar granule cell migration and neurite outgrowth by different domains in the fibronectin type III repeats. *J Cell Biol* 116:1475–1486. doi:10.1083/jcb.116.6.1475

Irala D, Wang S, Sakers K, Nagendren L, Ulloa-Severino FP, Bindu DS, Eroglu C. 2023. Astrocyte-Secreted Neurocan Controls Inhibitory Synapse Formation and Function. *bioRxiv* 2023.04.03.535448. doi:10.1101/2023.04.03.535448

Ishii M, Maeda N. 2008. Oversulfated Chondroitin Sulfate Plays Critical Roles in the Neuronal Migration in the Cerebral Cortex. *J Biol Chem* 283:32610–32620. doi:10.1074/jbc.M806331200

Jossin Y. 2020. Molecular mechanisms of cell polarity in a range of model systems and in migrating neurons. *Molecular and Cellular Neuroscience* 23.

Jossin Y, Cooper JA. 2011. Reelin, Rap1 and N-cadherin orient the migration of multipolar neurons in the developing neocortex. *Nat Neurosci* 14:697–703. doi:10.1038/nn.2816

Kanda Y. 2013. Investigation of the freely available easy-to-use software 'EZR' for medical statistics. *Bone Marrow Transplant* 48:452–458. doi:10.1038/bmt.2012.244

Katoh K, Standley DM. 2013. MAFFT multiple sequence alignment software version 7: improvements in performance and usability. *Mol Biol Evol* 30:772–780. doi:10.1093/molbev/mst010

Kriegstein A, Alvarez-Buylla A. 2009. The glial nature of embryonic and adult neural stem cells. *Annu Rev Neurosci* 32:149–184. doi:10.1146/annurev.neuro.051508.135600

Laskowski RA, Jabłońska J, Pravda L, Vařeková RS, Thornton JM. 2018. PDBsum: Structural summaries of PDB entries. *Protein Sci* 27:129–134. doi:10.1002/pro.3289

Lochter A, Vaughan L, Kaplony A, Prochiantz A, Schachner M, Faissner A. 1991. J1/tenascin in substrate-bound and soluble form displays contrary effects on neurite outgrowth. *Journal of Cell Biology* 113:1159–1171. doi:10.1083/jcb.113.5.1159

Long KR, Newland B, Florio M, Kalebic N, Langen B, Kolterer A, Wimberger P, Huttner WB. 2018. Extracellular Matrix Components HAPLN1, Lumican, and Collagen I Cause Hyaluronic Acid-Dependent Folding of the Developing Human Neocortex. *Neuron* 99:702-719.e6. doi:10.1016/j.neuron.2018.07.013

Lundell A, Olin AI, Mörgelin M, al-Karadaghi S, Aspberg A, Logan DT. 2004. Structural Basis for Interactions between Tenascins and Lectican C-Type Lectin Domains. *Structure* 12:1495–1506. doi:10.1016/j.str.2004.05.021

Maeda N, Ishii M, Nishimura K, Kamimura K. 2011. Functions of Chondroitin Sulfate and Heparan Sulfate in the Developing Brain. *Neurochem Res* 36:1228–1240. doi:10.1007/s11064-010-0324-y

Meijering E, Jacob M, Sarria J-CF, Steiner P, Hirling H, Unser M. 2004. Design and validation of a tool for neurite tracing and analysis in fluorescence microscopy images. *Cytometry A* 58:167–176. doi:10.1002/cyto.a.20022

Miller B, Sheppard AM, Bicknese AR, Pearlman AL. 1995. Chondroitin sulfate proteoglycans in the developing cerebral cortex: The distribution of neurocan distinguishes forming afferent and efferent

axonal pathways. *J Comp Neurol* 355:615–628. doi:10.1002/cne.903550410

Mirdita M, Schütze K, Moriwaki Y, Heo L, Ovchinnikov S, Steinegger M. 2022. ColabFold: making protein folding accessible to all. *Nat Methods* 19:679–682. doi:10.1038/s41592-022-01488-1

Miyata S, Kitagawa H. 2017. Formation and remodeling of the brain extracellular matrix in neural plasticity: Roles of chondroitin sulfate and hyaluronan. *Biochim Biophys Acta Gen Subj* 1861:2420–2434. doi:10.1016/j.bbagen.2017.06.010

Miyata S, Komatsu Y, Yoshimura Y, Taya C, Kitagawa H. 2012. Persistent cortical plasticity by upregulation of chondroitin 6-sulfation. *Nat Neurosci* 15:414–422. doi:10.1038/nn.3023

Mubuchi A, Katsumoto S, Tsuboi M, Ishikawa H, Nomura Y, Higashi K, Miyata S. 2022. Isolation and structural characterization of bioactive glycosaminoglycans from the green-lipped mussel Perna canaliculus. *Biochemical and Biophysical Research Communications* 612:50–56. doi:10.1016/j.bbrc.2022.04.095

Nakao N, Hiraiwa N, Yoshiki A, Ike F, Kusakabe M. 1998. Tenascin-C promotes healing of Habu-snake venom-induced glomerulonephritis: studies in knockout congenic mice and in culture. *Am J Pathol* 152:1237–1245.

Namba T, Funahashi Y, Nakamuta S, Xu C, Takano T, Kaibuchi K. 2015. Extracellular and Intracellular Signaling for Neuronal Polarity. *Physiological Reviews* 95:995–1024. doi:10.1152/physrev.00025.2014

Namba T, Kibe Y, Funahashi Y, Nakamuta S, Takano T, Ueno T, Shimada A, Kozawa S, Okamoto M, Shimoda Y, Oda K, Wada Y, Masuda T, Sakakibara A, Igarashi M, Miyata T, Faivre-Sarrailh C, Takeuchi K, Kaibuchi K. 2014. Pioneering Axons Regulate Neuronal Polarization in the Developing Cerebral Cortex. *Neuron* 81:814–829. doi:10.1016/j.neuron.2013.12.015

Noctor SC, Martínez-Cerdeño V, Ivic L, Kriegstein AR. 2004. Cortical neurons arise in symmetric and asymmetric division zones and migrate through specific phases. *Nat Neurosci* 7:136–144. doi:10.1038/nn1172

Ohtaka-Maruyama C, Okamoto M, Endo K, Oshima M, Kaneko N, Yura K, Okado H, Miyata T, Maeda N. 2018. Synaptic transmission from subplate neurons controls radial migration of neocortical neurons. *Science* 360:313–317. doi:10.1126/science.aar2866

Ohtsuka M, Sato M, Miura H, Takabayashi S, Matsuyama M, Koyano T, Arifin N, Nakamura S, Wada K, Gurumurthy CB. 2018. i-GONAD: a robust method for in situ germline genome engineering using CRISPR nucleases. *Genome Biol* 19:25. doi:10.1186/s13059-018-1400-x

Ohya T, Kaneko Y. 1970. Novel hyaluronidase from streptomyces. *Biochim Biophys Acta* 198:607–609. doi:10.1016/0005-2744(70)90139-7

Pollen AA, Nowakowski TJ, Chen J, Retallack H, Sandoval-Espinosa C, Nicholas CR, Shuga J, Liu SJ, Oldham MC, Diaz A, Lim DA, Leyrat AA, West JA, Kriegstein AR. 2015. Molecular Identity of Human Outer Radial Glia during Cortical Development. *Cell* 163:55–67. doi:10.1016/j.cell.2015.09.004

785 Polleux F, Morrow T, Ghosh A. 2000. Semaphorin 3A is a chemoattractant for cortical apical dendrites.
786 *Nature* 404:567–573. doi:10.1038/35007001
787 Rauch U, Clement A, Retzler C, Fröhlich L, Fässler R, Göhring W, Faissner A. 1997. Mapping of a defined
788 neurocan binding site to distinct domains of tenascin-C. *J Biol Chem* 272:26905–26912.
789 doi:10.1074/jbc.272.43.26905
790 Rauch U, Feng K, Zhou XH. 2001. Neurocan: a brain chondroitin sulfate proteoglycan. *Cell Mol Life Sci*
791 58:1842–1856. doi:10.1007/PL00000822
792 Rauch U, Karthikeyan L, Maurel P, Margolis RU, Margolis RK. 1992. Cloning and primary structure of
793 neurocan, a developmentally regulated, aggregating chondroitin sulfate proteoglycan of brain.
794 *Journal of Biological Chemistry* 267:19536–19547. doi:10.1016/S0021-9258(18)41808-X
795 Reinhard J, Brösicke N, Theocharidis U, Faissner A. 2016. The extracellular matrix niche microenvironment
796 of neural and cancer stem cells in the brain. *Int J Biochem Cell Biol* 81:174–183.
797 doi:10.1016/j.biocel.2016.05.002
798 Rigato F, Garwood J, Calco V, Heck N, Faivre-Sarrailh C, Faissner A. 2002. Tenascin-C Promotes Neurite
799 Outgrowth of Embryonic Hippocampal Neurons through the Alternatively Spliced Fibronectin Type
800 III BD Domains via Activation of the Cell Adhesion Molecule F3/Contactin. *J Neurosci* 22:6596–
801 6609. doi:10.1523/JNEUROSCI.22-15-06596.2002
802 Robert X, Gouet P. 2014. Deciphering key features in protein structures with the new ENDscript server.
803 *Nucleic Acids Res* 42:W320-324. doi:10.1093/nar/gku316
804 Sakurai N, Nishio S, Akiyama Y, Miyata S, Oshima K, Nadano D, Matsuda T. 2018. Apical-to-basolateral
805 transepithelial transport of cow's milk caseins by intestinal Caco-2 cell monolayers: MS-based
806 quantitation of cellularly degraded α- and β-casein fragments. *J Biochem* 164:113–125.
807 doi:10.1093/jb/mvy034
808 Sirko S, von Holst A, Wizenmann A, Götz M, Faissner A. 2007. Chondroitin sulfate glycosaminoglycans
809 control proliferation, radial glia cell differentiation and neurogenesis in neural stem/progenitor cells.
810 *Development* 134:2727–2738. doi:10.1242/dev.02871
811 Skupien A, Konopka A, Trzaskoma P, Labus J, Gorlewicz A, Swiech L, Babraj M, Dolezyczek H, Figiel I,
812 Ponimaskin E, Wlodarczyk J, Jaworski J, Wilczynski GM, Dzwonek J. 2014. CD44 regulates
813 dendrite morphogenesis through Src tyrosine kinase-dependent positioning of the Golgi. *J Cell Sci*
814 127:5038–5051. doi:10.1242/jcs.154542
815 Sugitani K, Egorova D, Mizumoto S, Nishio S, Yamada S, Kitagawa H, Oshima K, Nadano D, Matsuda T,
816 Miyata S. 2021. Hyaluronan degradation and release of a hyaluronan-aggrecan complex from
817 perineuronal nets in the aged mouse brain. *Biochim Biophys Acta Gen Subj* 1865:129804.
818 doi:10.1016/j.bbagen.2020.129804
819 Tabata H, Nakajima K. 2003. Multipolar migration: the third mode of radial neuronal migration in the
820 developing cerebral cortex. *J Neurosci* 23:9996–10001.
821 Takechi M, Oshima K, Nadano D, Kitagawa H, Matsuda T, Miyata S. 2020. A pericellular hyaluronan matrix

822 is required for the morphological maturation of cortical neurons. *Biochim Biophys Acta Gen Subj*
823 1864:129679. doi:10.1016/j.bbagen.2020.129679
824 Taverna E, Götz M, Huttner WB. 2014. The Cell Biology of Neurogenesis: Toward an Understanding of the
825 Development and Evolution of the Neocortex. *Annu Rev Cell Dev Biol* 30:465–502.
826 doi:10.1146/annurev-cellbio-101011-155801
827 Telley L, Govindan S, Prados J, Stevant I, Nef S, Dermitzakis E, Dayer A, Jabaudon D. 2016. Sequential
828 transcriptional waves direct the differentiation of newborn neurons in the mouse neocortex. *Science*
829 351:1443–1446. doi:10.1126/science.aad8361
830 Tina KG, Bhadra R, Srinivasan N. 2007. PIC: Protein Interactions Calculator. *Nucleic Acids Res* 35:W473-
831 476. doi:10.1093/nar/gkm423
832 Tucker RP, Chiquet-Ehrismann R. 2015. Tenascin-C: Its functions as an integrin ligand. *The International*
833 *Journal of Biochemistry & Cell Biology* 65:165–168. doi:10.1016/j.biocel.2015.06.003
834 Turk BE, Huang LL, Piro ET, Cantley LC. 2001. Determination of protease cleavage site motifs using
835 mixture-based oriented peptide libraries. *Nat Biotechnol* 19:661–667. doi:10.1038/90273
836 von Holst A, Sirko S, Faissner A. 2006. The unique 473HD-Chondroitinsulfate epitope is expressed by radial
837 glia and involved in neural precursor cell proliferation. *J Neurosci* 26:4082–4094.
838 doi:10.1523/JNEUROSCI.0422-06.2006
839 Yamaguchi Y. 2000. Lecticans: organizers of the brain extracellular matrix. *CMLS, Cell Mol Life Sci* 57:276–
840 289. doi:10.1007/PL00000690
841 Yi JJ, Barnes AP, Hand R, Polleux F, Ehlers MD. 2010. TGF-beta signaling specifies axons during brain
842 development. *Cell* 142:144–157. doi:10.1016/j.cell.2010.06.010
843 Yoshinaga S, Shin M, Kitazawa A, Ishii K, Tanuma M, Kasai A, Hashimoto H, Kubo K, Nakajima K. 2021.
844 Comprehensive characterization of migration profiles of murine cerebral cortical neurons during
845 development using FlashTag labeling. *iScience* 24:102277. doi:10.1016/j.isci.2021.102277
846 Zhou X-H, Brakebusch C, Matthies H, Oohashi T, Hirsch E, Moser M, Krug M, Seidenbecher CI, Boeckers
847 TM, Rauch U, Buettner R, Gundelfinger ED, Fässler R. 2001. Neurocan Is Dispensable for Brain
848 Development. *Mol Cell Biol* 21:5970–5978. doi:10.1128/MCB.21.17.5970-5978.2001
849 Zimmermann DR, Dours-Zimmermann MT. 2008. Extracellular matrix of the central nervous system: from
850 neglect to challenge. *Histochem Cell Biol* 130:635–653. doi:10.1007/s00418-008-0485-9
851
852

Table 1. List of proteins identified from GFP-NCAN and negative control resins

GFP-NCAN resin

Protein name	No. of peptide
Neurocan core protein	34
Tenascin	22
Tubulin alpha-1A chain	18
Tubulin beta-2B chain	17
Tubulin beta-5 chain	16
Actin, cytoplasmic 2	11
Actin, cytoplasmic 1	10
Tubulin beta-6 chain	9
Elongation factor 1-alpha 1	8
Crk-like protein	6
Profilin-2	4
Eukaryotic translation initiation factor 3 subunit L	4
Histone deacetylase 6	4
40S ribosomal protein SA	4
Casein kinase II subunit alpha	3
Macrophage migration inhibitory factor	3
Eukaryotic translation initiation factor 3 subunit E	3
Keratin, type II cytoskeletal 1b	3

Negative control resin

Protein name	No. of peptide
Tubulin beta-2B chain	21
Tubulin beta-5 chain	17
Tubulin beta-3 chain	15
Tubulin beta-6 chain	15
Tubulin alpha-1A chain	13
Actin, cytoplasmic 2	10
Elongation factor 1-alpha 1	5
Macrophage migration inhibitory factor	5
Crk-like protein	4
Keratin, type II cytoskeletal 1	4
Peroxiredoxin-1	3
L-lactate dehydrogenase A chain	3
Keratin, type I cytoskeletal 10	3
Hemoglobin subunit alpha	3
Hemoglobin subunit beta-1	3
Keratin, type II cytoskeletal 1b	3

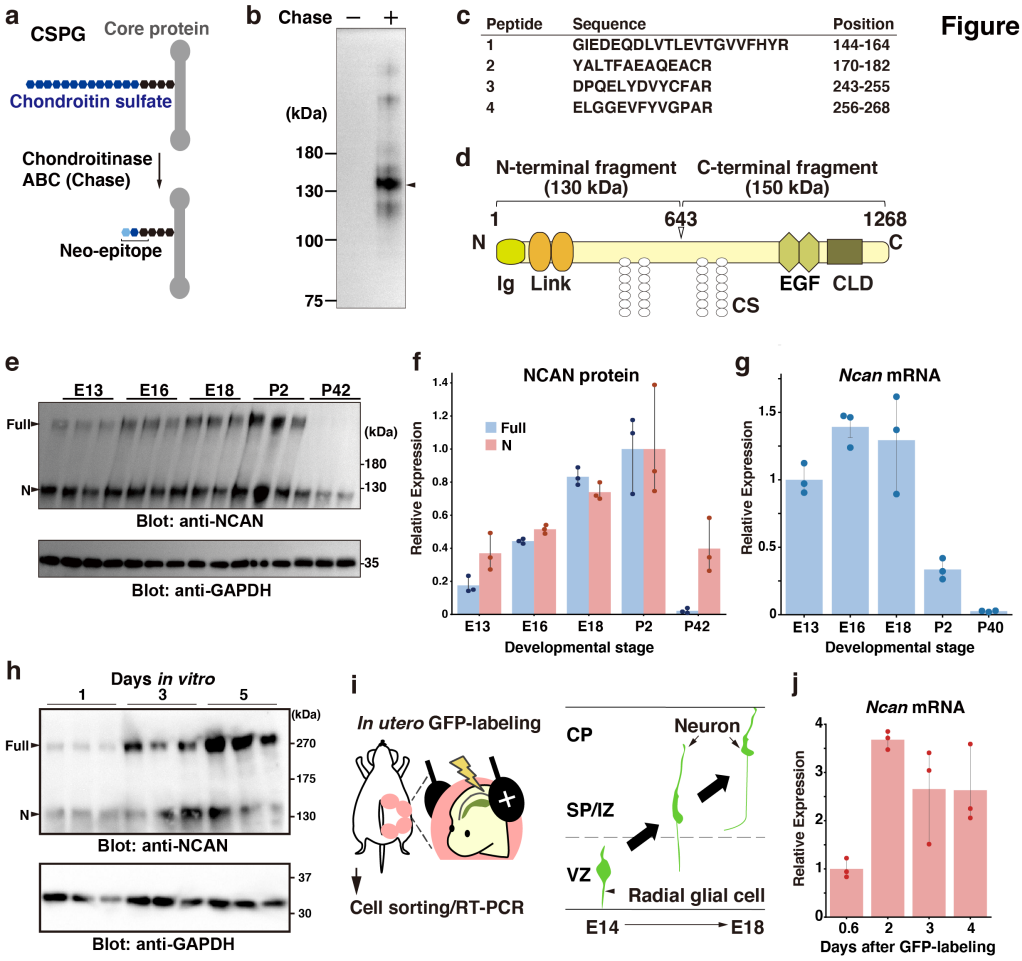

Figure 1. NCAN is a major CSPG produced by developing cortical neurons. (a) Detection of the neoepitope of CSPGs after digestion with chondroitinase ABC (Chase). (b) Immunoblotting of the neoepitope from undigested (Chase -) and digested (Chase +) cerebral cortex lysates prepared at E18. The arrowhead indicates the major CSPG at 130 kDa. (c) List of peptide fragments identified from the 130-kDa band. Positions indicate the amino acid number in full-length NCAN. (d) Domain structure of mouse NCAN. Ig: immunoglobulin-like domain, Link: hyaluronan-binding link module, EGF: epidermal growth factor-like repeat, CLD: C-type lectin domain, CS: chondroitin sulfate chain. (**e, f**) NCAN expression in the developing cerebral cortex from E13 to postnatal day (P) 42. The arrowheads indicate the full-length and N-terminal fragment of NCAN. Values in (f) are normalized to GAPDH and represented relative to P2. N = 3 for each point. Mean ± SD. (**g**) Quantitative RT-PCR analysis of *Ncan* mRNA in the developing cerebral cortex. Values are normalized to *Gapdh* and represented relative to E13. N = 3 for each point. Mean ± SD. (**h**) Immunoblot analysis of NCAN in the cultured medium of primary cultured cortical neurons 1, 3, and 5 days after plating. (**i**) Experimental model for *in utero* labeling. Radial glial cells in the VZ were labeled with GFP on E14. GFP-positive cells were isolated 0.6–4 days later. (**j**) Expression of *Ncan* mRNA in GFP-labeled cells isolated on the indicated days after *in utero* electroporation. Values are normalized to *Gapdh* and represented relative to 0.6 days. N = 3 for each point. Mean ± SD.

Figure 1-figure supplement 1

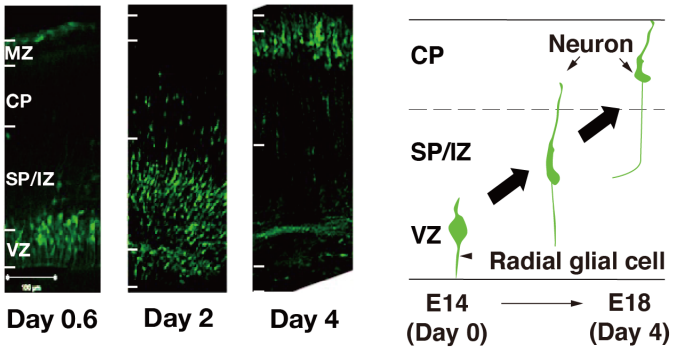

Figure 1-figure supplement 1. Location of GFP-positive cells 0.6, 2, and 4 days after *in utero* electroporation. Most GFP-positive cells are in the VZ on day 0.6. GFP-positive cells begin to migrate radially through the SP/IZ on day 2 and reach the CP on day 4. The scale bar represents 100 μm.

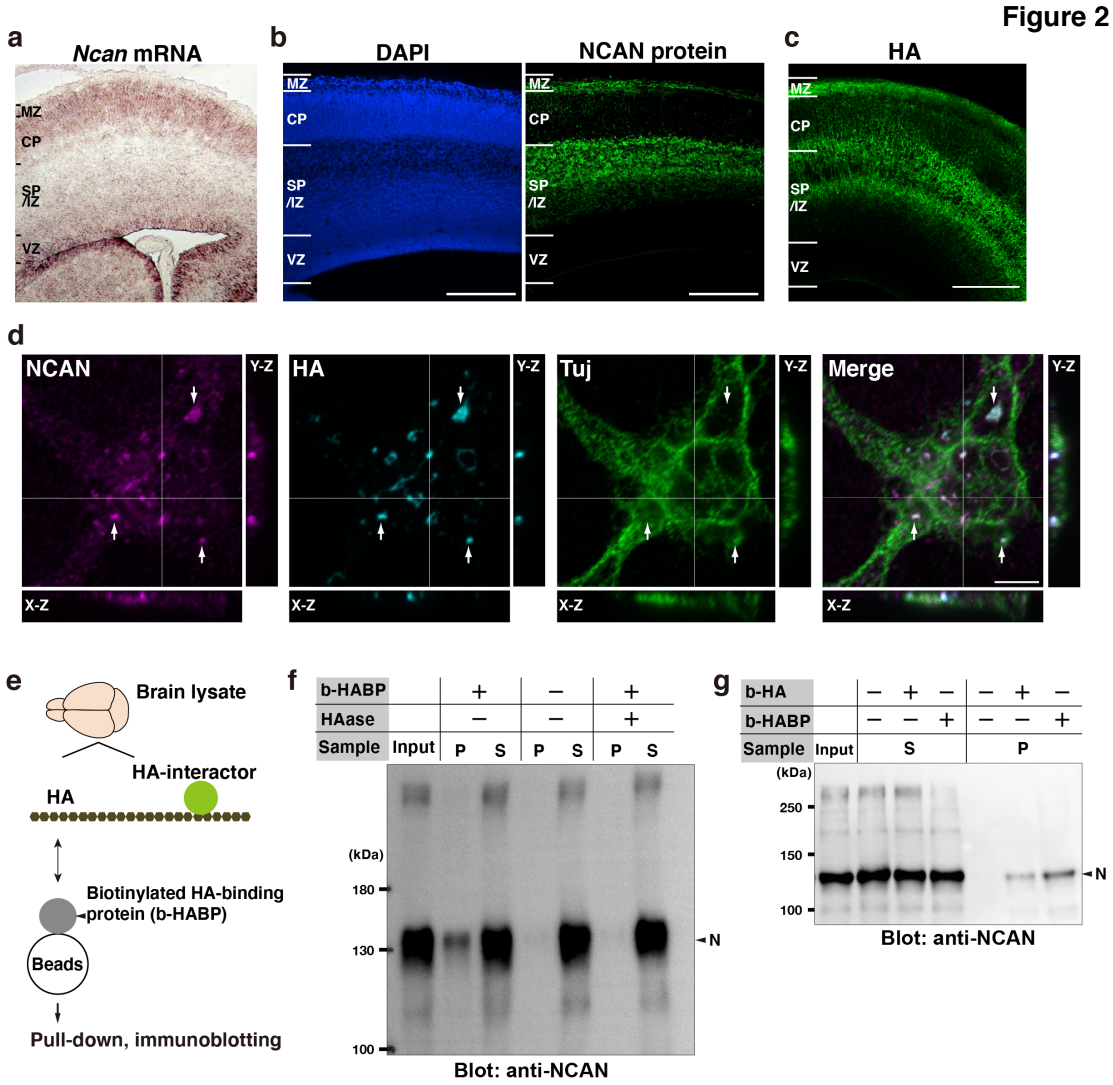

Figure 2. Neuron-derived NCAN forms a pericellular matrix with HA. (**a**) *In situ* hybridization analysis of *Ncan* mRNA on the E16 cerebral cortex. (**b**) Localization of NCAN protein (green) in the E16 cerebral cortex. Nuclei were counterstained with DAPI (blue). (**c**) Distribution of HA (green) visualized by the biotinylated HA-binding protein (b-HABP) in the E16 cerebral cortex. (**d**) High magnification views of a Tuj-1-positive primary cultured cortical neuron (green) 5 days after plating. White arrows indicate the co-localization of NCAN (magenta) and HA (cyan). Orthogonal projections in the X-Z and Y-Z planes taken along the white lines showed the localization of NCAN and HA at the adhesion sites between the neuron and culture substrate. (**e**) Schema of the pull-down assay for analyzing binding between endogenous HA and its interactors. (**f**) Immunoblotting of the input, precipitate (P), and supernatant (S) with an anti-NCAN antibody. NCAN was precipitated with HA by adding b-HABP (b-HABP +). NCAN was not precipitated without b-HABP (b-HABP -) or after digestion with hyaluronidase (HAase +). (**g**) Co-precipitation of NCAN with exogenously added biotinylated HA (b-HA +) or endogenous HA (b-HABP +). Scale bars represent 200 μm (a, c) and 5 μm (d).

Figure 2-figure supplement 1

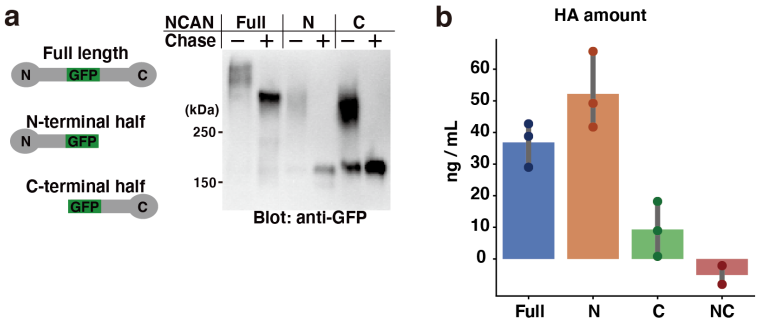

Figure 2-figure supplement 1. Pull-down assay of HA with recombinant GFP-fused NCAN. (**a**) Recombinant expression of GFP-fused full-length, N-terminal, and C-terminal half of NCAN. The culture medium of transfected HEK293 cells was digested with chondroitinase ABC (Chase) and analyzed by immunoblotting with an anti-GFP antibody. (**b**) Quantification of precipitated HA by the full-length, N-terminal, and C-terminal half of NCAN. A negative control experiment (NC) was conducted without NCAN. N = 3 for each point. Mean ± SD.

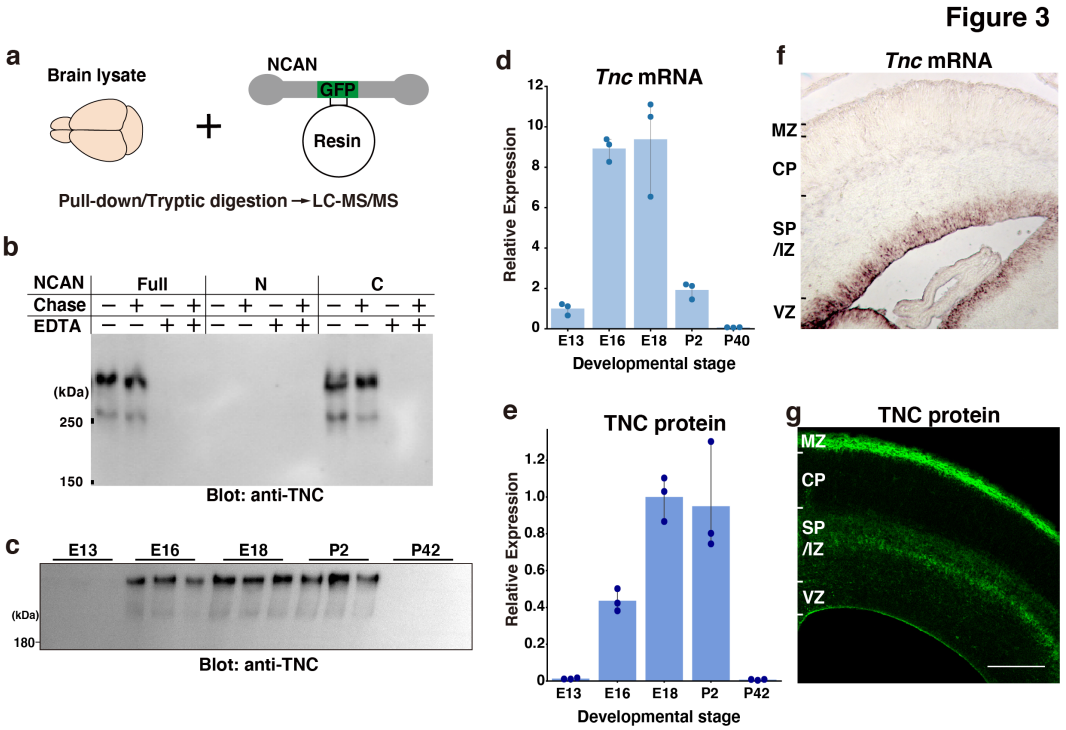

Figure 3. Screening of the interacting partners of NCAN. (**a**) Schematic of the pull-down assay to identify NCAN-interacting partners. (**b**) Co-precipitation of TNC with the full-length and C-terminal half of NCAN. Interactions between NCAN and TNC disappeared following the addition of EDTA but were not affected by Chase digestion. The N-terminal half of NCAN did not bind to TNC. (**c, e**) TNC expression in the developing cerebral cortex from E13 to postnatal day (P) 42. Values in (e) are normalized to GAPDH and represented relative to P2. N = 3 for each point. Mean ± SD. (**d**) Quantitative RT-PCR analysis of *Tnc* mRNA in the developing cerebral cortex. Values are normalized to *Gapdh* and represented relative to E13. N = 3 for each point. Mean ± SD. (**f, g**) *In situ* hybridization analysis of *Tnc* mRNA (f) and immunohistochemical localization of TNC protein (g) in the E16 cerebral cortex. The scale bar represents 200 μm.

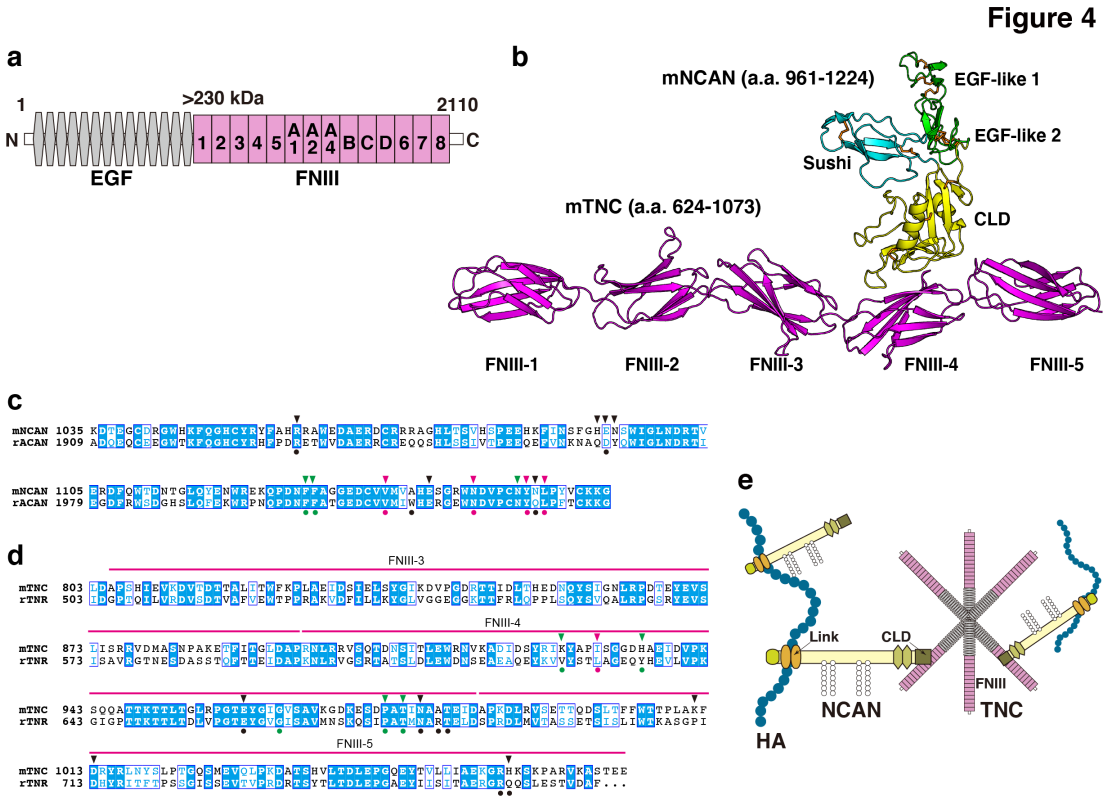

Figure 4. Alphafold2 prediction of the NCAN-TNC complex. (**a**) Domain structure of mouse (m) TNC. EGF: epidermal growth factor-like repeat, FNIII: fibronectin type-III domain. (**b**) Five predicted complex models of the mNCAN and mTNC were generated using AlphaFold2 multimer implemented in ColabFold, and the best-predicted complex was shown. (**c**, **d**). Sequence alignments of CLD of mNCAN and rat (r) ACAN (c) and FNIII-3-5 of mTNC and rTNR (d). Circles under alignments indicate the key residues of the rACAN-rTNR complex. Triangles over alignments indicate the residues in the interface of mNCAN-mTNC. Green and magenta circles/triangles are the residues involved in the interaction between L4 loop of CLD and βC, F, G strands of FNIII-4 and β6, 7 strands of CLD and CC' loop of FNIII-4, respectively. Black circles/triangles indicate residues involved in the interaction between CLD and FNIII-4-5 linker region/FG loop of FNIII-5. (**e**) Model for forming the ternary complex of NCAN, HA, and TNC.

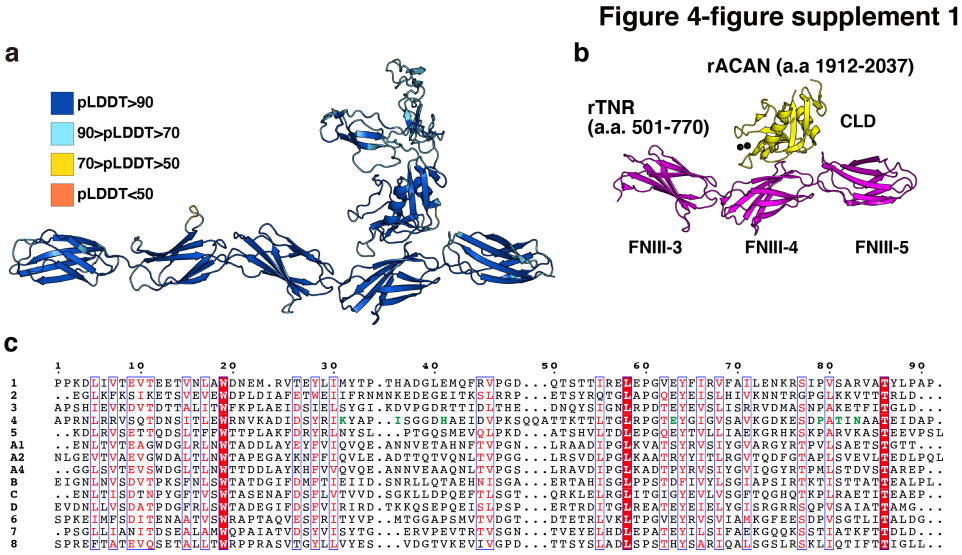

Figure 4-figure supplement 1. Alphafold2 prediction of NCAN-TNC complex. (**a**) Model confidence of NCAN-TNC complex. Each residue is colored by pLDDT score, and a high pLDDT score indicates high accuracy. (**b**) Crystal structure of rat (r) ACAN-TNR complex (PDB ID: 1TDQ). Each domain is colored the same as in Figure 4c. (**c**) Sequence alignments of fourteen FNIII of mTNC. Green letters indicate residues involved in the interaction between FNIII-4 and CLD of NCAN.

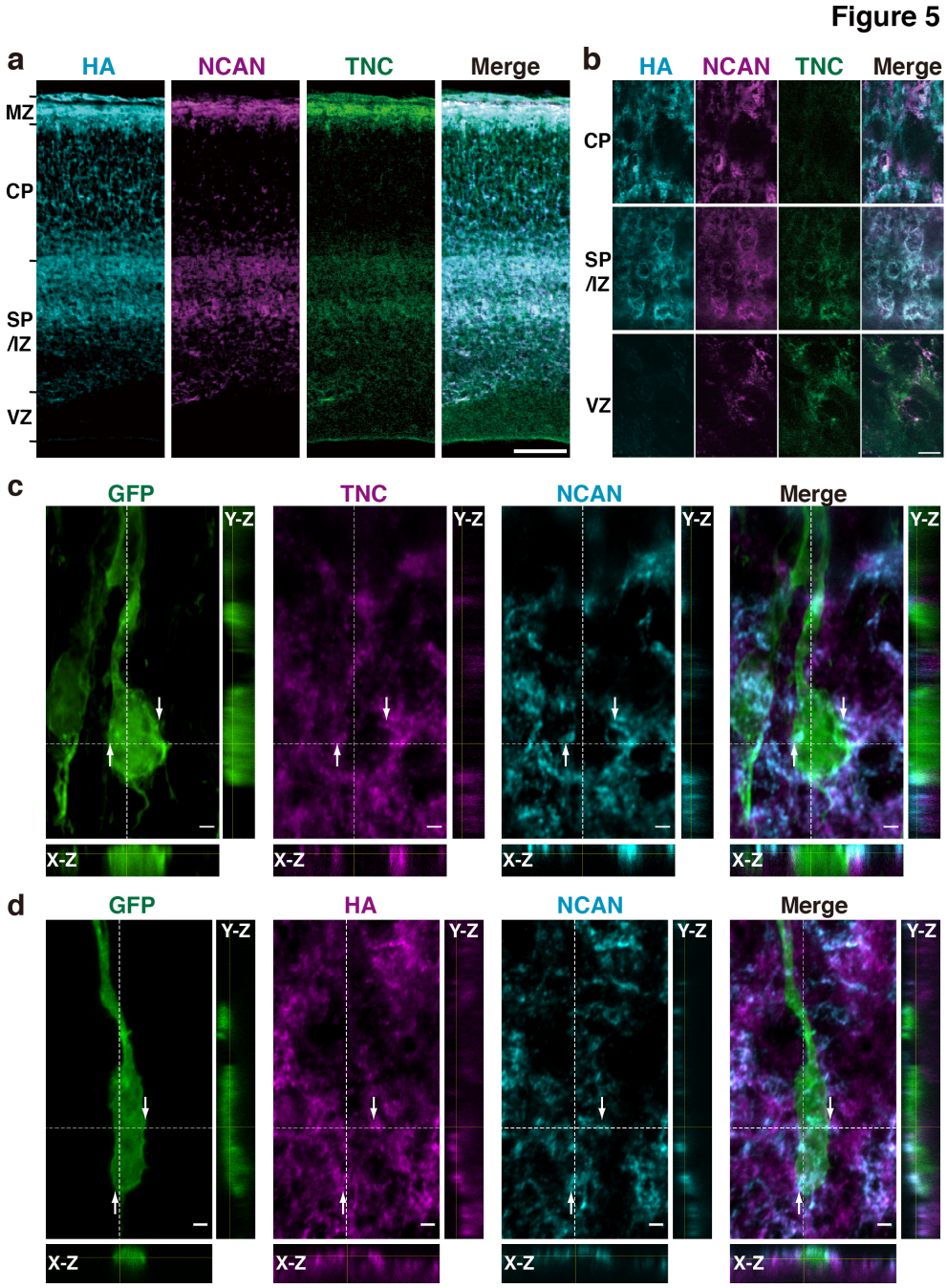

929
930
931 **Figure 5.** HA, NCAN, and TNC form the ternary complex in the developing cerebral cortex. (**a**) Triple
932 staining of the E17 mouse cerebral cortex with HA (cyan), NCAN (magenta), and TNC (green). (**b**) High
933 magnification images show the co-localization of the three components in the upper part of the SP/IZ but not
934 in the CP or VZ. (**c, d**) Localization of TNC (c, magenta), NCAN (c, d, cyan), and HA (d, magenta) around
935 GFP-labeled bipolar neurons (green) in the upper SP/IZ at E17, three days after *in utero* labeling. Orthogonal
936 views taken along the white dashed lines showed the contact between the ternary complex and the surface of
937 bipolar neurons, as indicated by the arrows. Scale bars represent 100 μm (a), 5 μm (b), and 2 μm (c, d).
938

Figure 6

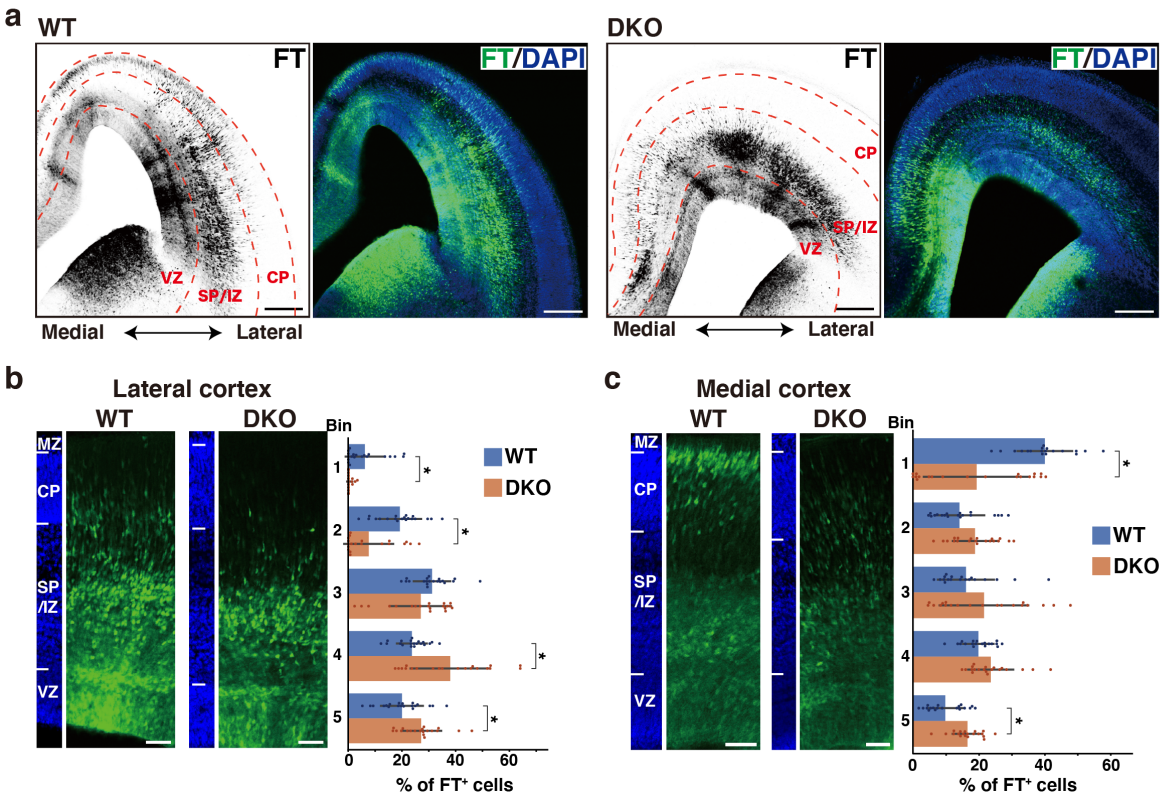

Figure 6. Defects in NCAN and TNC retards neuronal migration. (**a**) Low magnification images of FT-labeled cells (black or green) in WT and DKO mouse coronal sections at E16. Nuclei were counterstained with DAPI (blue). (**b, c**) Radial distribution of FT-labeled cells (green) in the lateral (b) and medial (c) cortices of WT and DKO mice at E16. A quantitative analysis of migration profiles across the cortex is shown on the right. The cerebral cortex is divided into five equal areas (bins 1–5) from the pia to the ventricle, and the proportion of FT-labeled cells in each bin was calculated. The nuclei staining images (blue) on the left illustrate the boundaries of the cortical layers. N = 19–20 mice per group. Mean ± SD; *$p < 0.05$; Student's t-test. Scale bars represent 200 μm (a) and 50 μm (b, c).

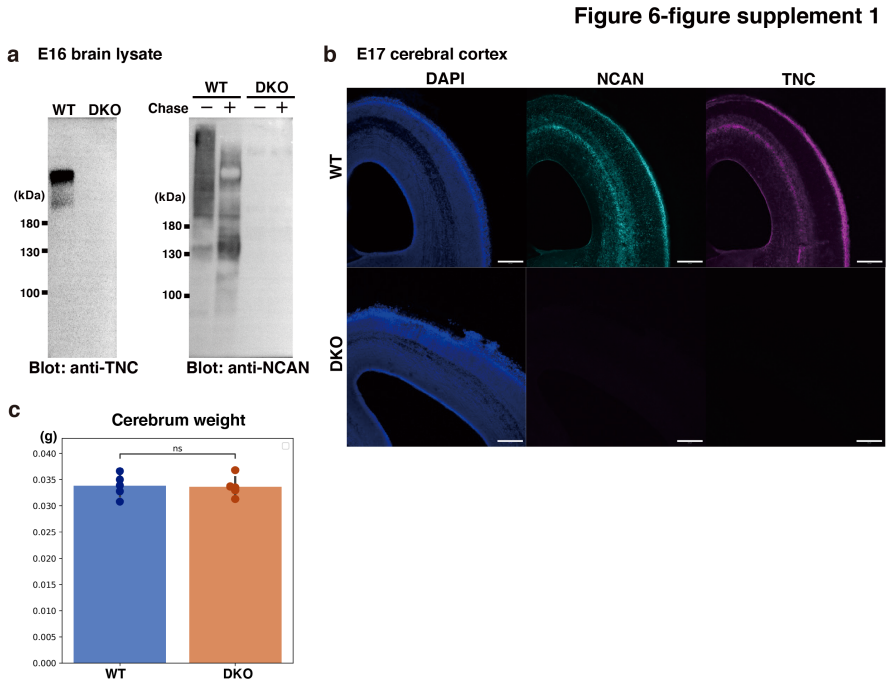

949

950 **Figure 6-figure supplement 1.** Characterization of DKO. (**a**) Immunoblot analysis of TNC and NCAN from
951 WT and DKO mouse cerebral cortex lysates digested with or without chondroitinase ABC (Chase). (**b**)
952 Immunostaining of NCAN and TNC on coronal sections of WT and DKO mouse brains at E17. Scale bars
953 represent 200 µm. (**c**) No significant difference in cerebrum weights between WT and DKO mice at E16. N
954 = 5 mice per group. Mean ± SD; ns > 0.05; Student's t-test.

Figure 6-figure supplement 2

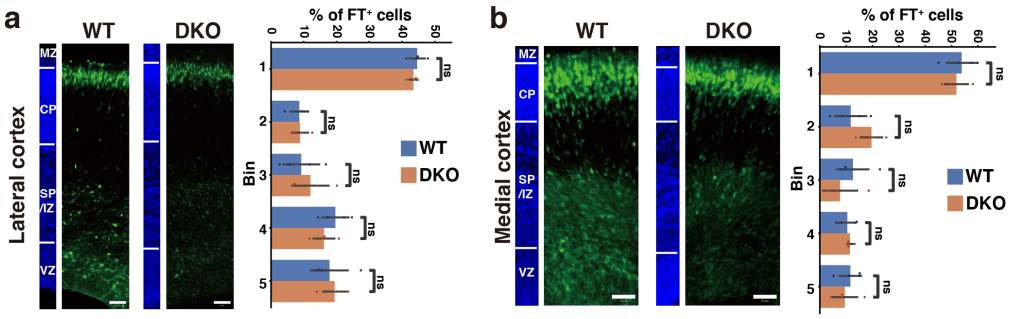

Figure 6-figure supplement 2. Restored neuronal migration in DKO mice after three days of labeling. (**a, b**) Radial distribution of FT-labeled cells (green) in the lateral (a) and medial (b) cortices of WT and DKO mice at E17. A quantitative analysis of migration profiles across the cortex is shown on the right. The nuclei staining images (blue) on the left illustrate the boundaries of the cortical layers. N = 4 mice per group. Mean ± SD; ns > 0.05; Student's t-test. Scale bars represent 50 µm.

Figure 6-figure supplement 3

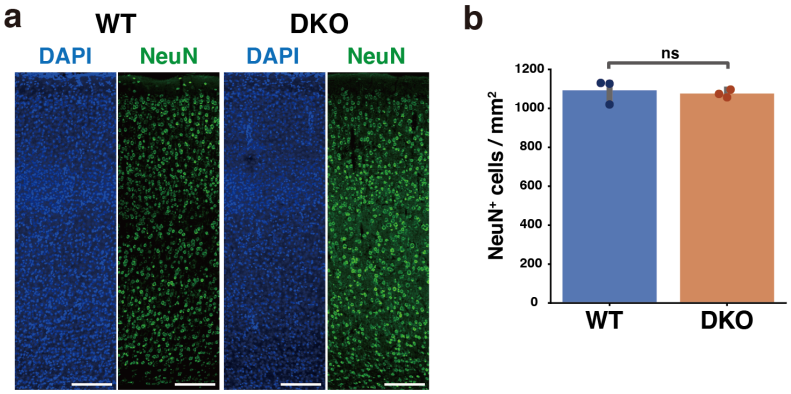

Figure 6-figure supplement 3. (**a**) Immunostaining of NeuN-positive neurons (green) in the cerebral cortices of WT and DKO at 4 weeks of age. Nuclei were counterstained with DAPI (blue). (**b**) Bar graphs show the numbers of NeuN-positive cells per mm^2. N = 3 mice per group. Mean ± SD; ns > 0.05; Student's t-test. The scale bar represents 200 μm (b).

Figure 6-figure supplement 4

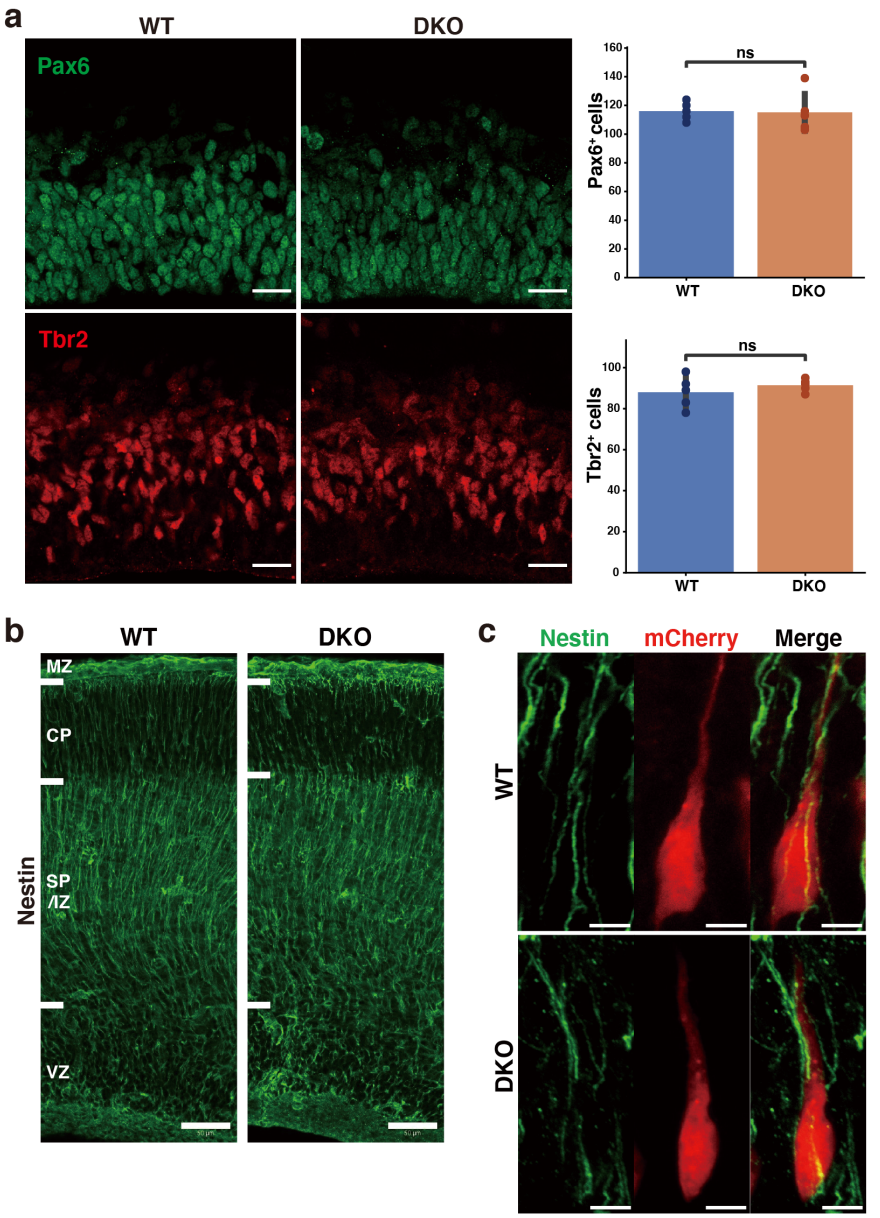

968

969 **Figure 6-figure supplement 4.** Histochemical analysis of radial glial cells, intermediate progenitor cells,
970 and the morphology of radial fibers in DKO mice. (**a**) Immunostaining of Pax6-positive radial glial cells
971 (green) and Tbr2-positive intermediate progenitor cells (red) in the VZ of WT and DKO cerebral cortices at
972 E16. Bar graphs show the numbers of Pax6- and Tbr2-positive cells per 150 × 150 μm^2. N = 5 mice per group.
973 Mean ± SD; ns > 0.05; Student' s t-test. (**b**) Immunostaining of nestin-positive radial fibers in WT and DKO
974 cerebral cortices at E16. (**c**) High magnification images of mCherry-positive bipolar neurons and radial fibers
975 in the WT and DKO at E16, 2 days after *in utero* labeling. Bipolar neurons in the SP/IZ-attached radial fiber,
976 irrespective of genotypes. Scale bars represent 20 μm (a), 50 μm (b), and 5 μm (c).

Figure 7

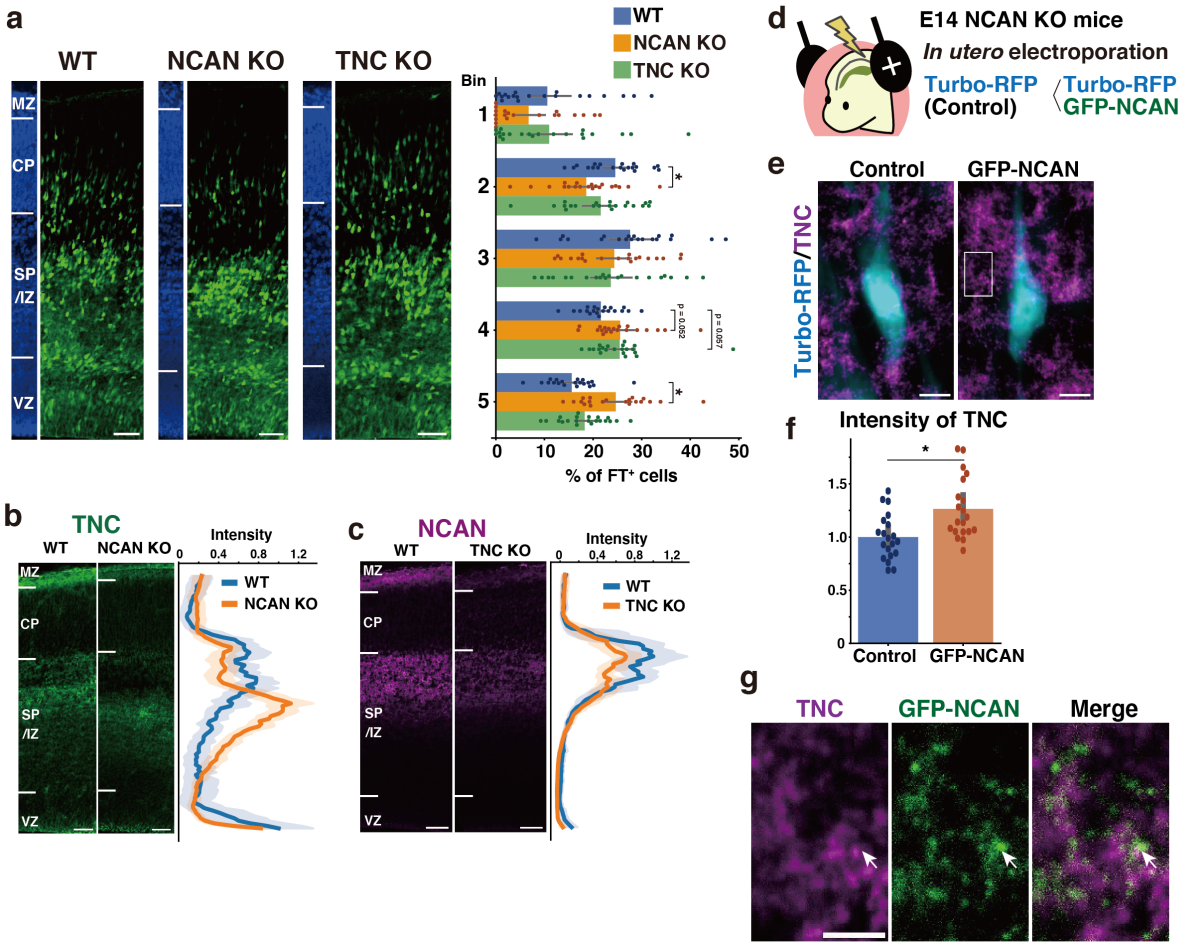

Figure 7. Single deletion of NCAN or TNC results in mild abnormalities in neuronal migration. (**a**) Radial distribution of FT-labeled cells (green) in the lateral cortices of WT, NCAN KO, and TNC KO mice at E16. A quantitative analysis of migration profiles across the cortex is shown on the right. The nuclei staining images (blue) on the left illustrate the boundaries of the cortical layers. N = 20-21 mice per group. Mean ± SD; *p < 0.05 vs. WT; Dunnett's test. (**b, c**) Localization of TNC in WT and NCAN KO mice at E16 (b). Localization of NCAN in WT and TNC KO mice at E16 (c). The normalized fluorescence intensity profiles of TNC and NCAN are shown on the right of the images. The maximum intensity value for WT mice was set to 1. N = 8-13 mice for each group. Mean ± SD (shaded area). (**d**) *In utero* electroporation of Turbo-RFP alone or with GFP-fused full-length NCAN (GFP-NCAN) into the NCAN KO brain at E16. (**e**) Immunostaining of TNC (magenta) around Turbo-RFP-positive neurons (cyan) 2 days after electroporation. (**f**) Staining intensity of TNC around the control and GFP-NCAN-expressing neuron. N = 20 images per group. Mean ± SD; *p < 0.05; Student's t-test. (**g**) High magnification of the boxed region in (e). The arrows indicate the juxtaposed localization of TNC (magenta) and GFP-NCAN (green). Scale bars represent 50 µm (a, b, c), 5 µm (e), and 2 µm (g).

Figure 7-figure supplement 1

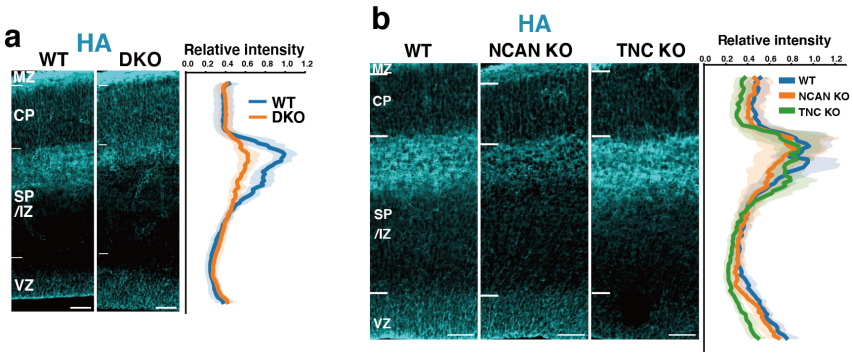

Figure 7-figure supplement 1. Localization of HA in WT, DKO, NCAN KO, and TNC KO mice. (**a**) Distribution patterns of HA in the E16 cerebral cortices of WT and DKO mice. The fluorescence intensity profile is shown on the right. The maximum intensity value for WT mice was set to 1. N = 11 mice for each group. Mean ± SD (shaded area). (**b**) Comparison of HA staining in the E16 cerebral cortices of WT, NCAN KO, and TNC KO mice. The normalized fluorescence intensity profiles of HA are shown on the right of the image. The maximum intensity value for WT mice was set to 1. N = 7-9 mice for each group. Mean ± SD (shaded area). Scale bars represent 50 μm.

Figure 8

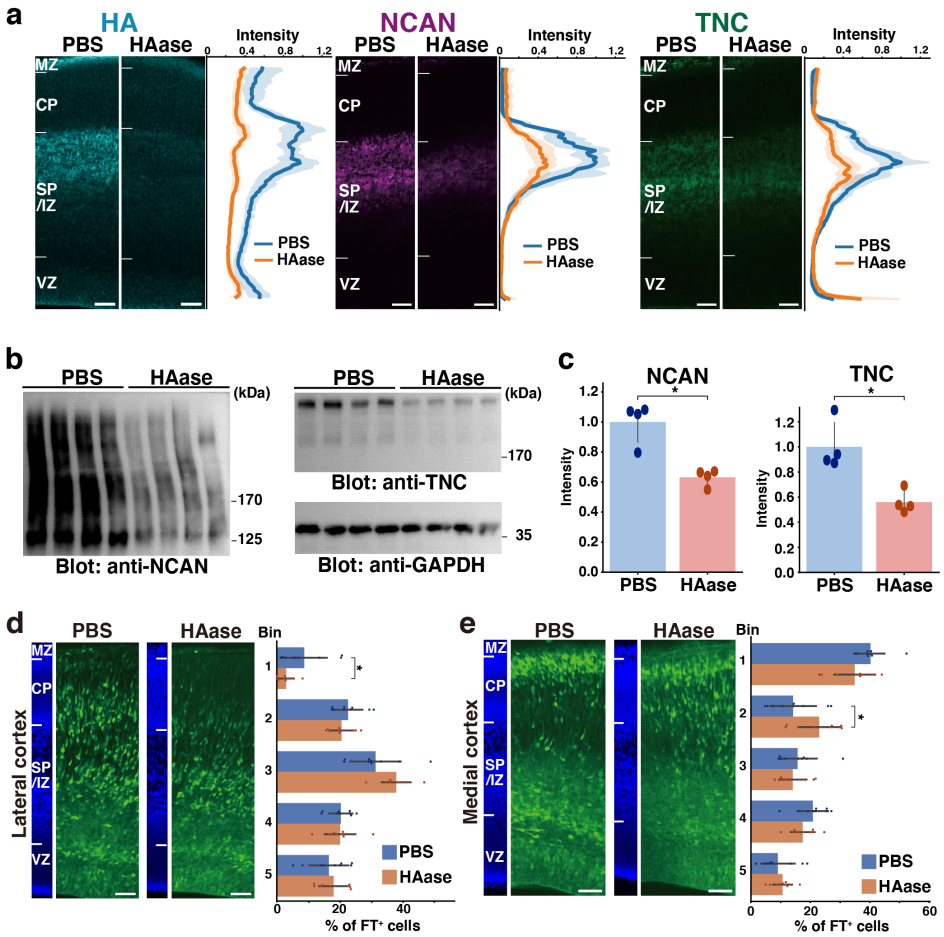

1001

1002 **Figure 8.** Transient disruption of the ternary complex by hyaluronidase injection. (**a**) Localization of HA,
1003 NCAN, and TNC in the cerebral cortex two days after intraventricular injection of PBS or hyaluronidase
1004 (HAase) at E14. The normalized fluorescence intensity profiles of HA, NCAN, and TNC are shown on the
1005 right of each image. The maximum intensity value for PBS-injected mice was set to 1. N = 5 mice for each
1006 group. Mean ± SD (shaded area). (**b**) Immunoblot analysis of NCAN and TNC in cerebral cortex lysates two
1007 days after intraventricular injection of PBS or HAase. The broadening of the NCAN band is due to the
1008 absence of chondroitinase ABC digestion. (**c**) The NCAN (left) and TNC (right) amounts were represented
1009 relative to the PBS-injected group. N = 4 mice per group. Mean ± SD; *p < 0.01; Student's t-test. (**d, e**)
1010 Distribution of FT-labeled cells (green) in the lateral (d) and medial (e) cortices two days after injection of
1011 PBS or HAase at E14. N = 9–10 mice per group. Mean ± SD; *p < 0.05; Student's t-test. Scale bars represent
1012 50 μm.

1013

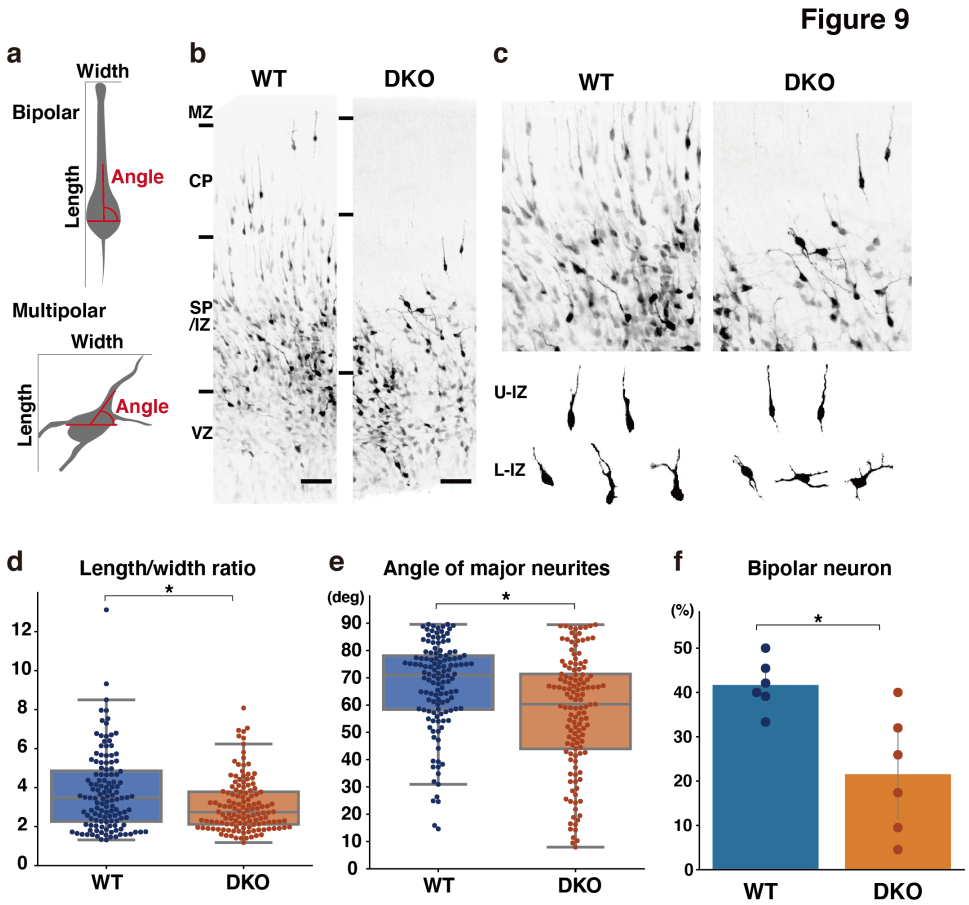

Figure 9. Delayed multipolar-to-bipolar transition in DKO mice. (**a**) Schematic of the morphological analysis. (**b, c**) Migration of mCherry-labeled cells in the WT and DKO cerebral cortices at E16, 53 h after *in utero* labeling (b). High magnification images of mCherry-labeled cells in the IZ (c). The images below show the morphology of neurons in the upper IZ (U-IZ) and lower IZ (L-IZ). (**d, e**) The length-to-width ratio (e) and the major neurite angle (f) of mCherry-positive neurons in WT and DKO mice. N = 128–134 cells from 6 mice per group. *$p < 0.05$; Student's t-test. (**f**) The proportion of bipolar neurons among mCherry-labeled neurons in the WT and DKO cortices. N = 6 mice per group. Mean ± SD; *$p < 0.05$; Student's t-test. Scale bars represent 50 μm (b).

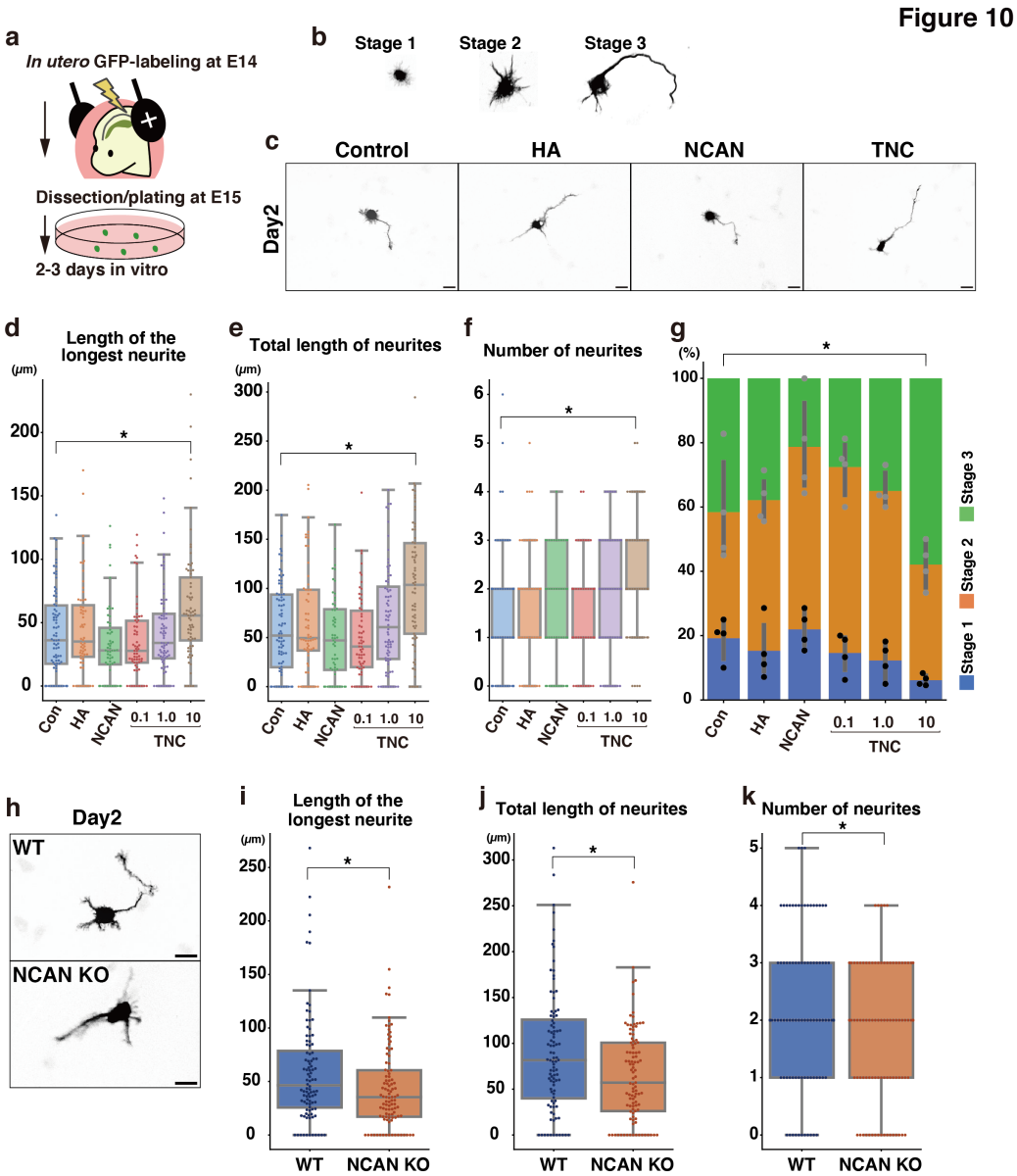

Figure 10. Morphological maturation of cortical neurons by TNC and NCAN. (**a**) Experimental model for *in utero* cell labeling and the primary neuronal culture. (**b**) Morphological stages of primary cultured cortical neurons. (**c**) Representative images of GFP-labeled neurons cultured for 2 days on cover glasses coated with the control substrate, poly-L-ornithine (POL), and 10 μg/mL of TNC, HA, and NCAN. (**d-f**) The length of the longest neurite (d), total length of neurites (e), and number of neurites (f) of neurons cultured on the indicated substrate for 2 days. N = 55–80 cells per condition. *$p < 0.05$ vs Control (Con); Dunnett's test. (**g**) The percentage of neurons with each morphological stage after culturing on the indicated substrate for 2 days. N = 4 wells per condition. Mean ± SD. *$p < 0.05$ vs Con for stage 1; Dunnett's test. (**h**) Representative images of GFP-labeled neurons derived from WT and NCAN KO mice cultured for 2 days on cover glasses coated with POL. (**i-k**) The length of the longest neurite (i), total length of neurites (j), and number of neurites (k) of WT and NCAN KO neurons cultured for 2 days. N = 96–101 cells per condition. *$p < 0.05$; Student's t-test. Scale bars represent 20 μm (c, h).

1037

Figure 10-figure supplement 1

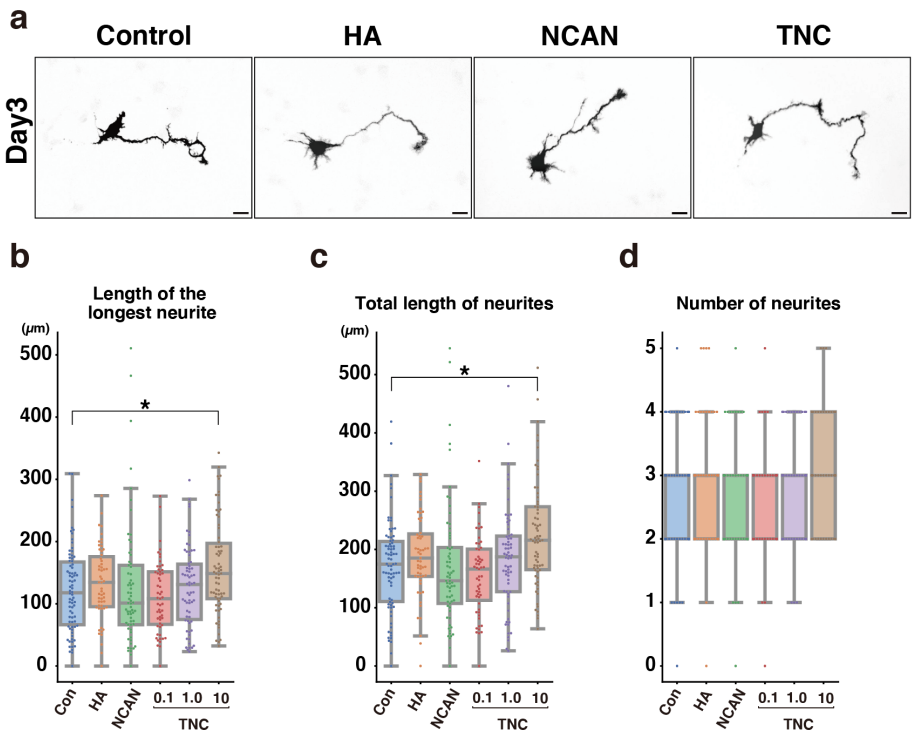

1038

1039 **Figure 10-figure supplement 1.** Morphological analysis of cortical neurons cultured for 3 days on cover
1040 glasses coated with HA, NCAN, and TNC. (**a**) Representative images of GFP-labeled neurons after
1041 culturing on the indicated substrate for 3 days. (**b-d**) The length of the longest neurite (b), total length of
1042 neurites (c), and number of neurites (d) of neurons cultured on the indicated substrate for 3 days. N = 55–
1043 78 cells per condition. *$p < 0.05$ vs Control (Con); Dunnett's test.

1044

Figure 10-figure supplement 2

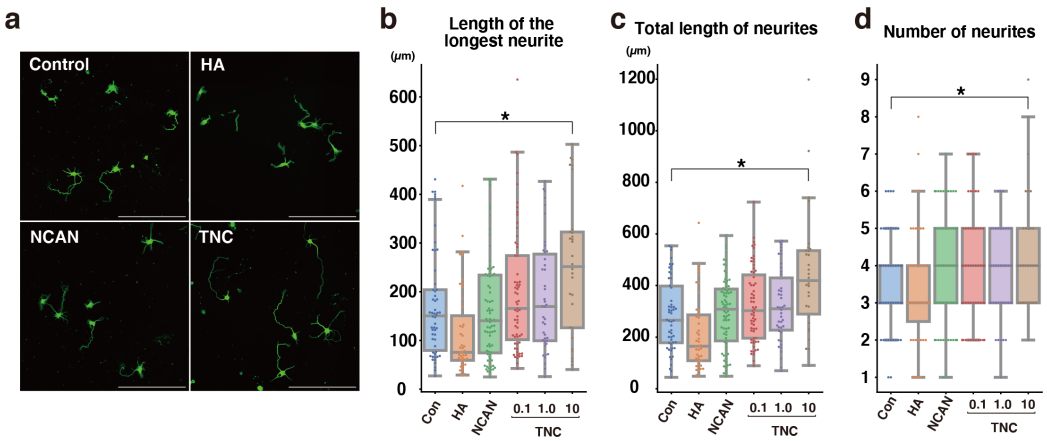

Figure 10-figure supplement 2. Neurite outgrowth analysis with anti-Tuj-1 antibody staining (**a**) Representative images of neurons stained with anti-Tuj-1 antibody after 3 days of culture on the indicated substrate. (**b-d**) The length of the longest neurite (b), total length of neurites (c), and number of neurites (d) of neurons. Neurites were analyzed using AutoNeuriteJ. N = 30–76 cells per condition. *$p < 0.05$ vs Control (Con); Dunnett's test.

Figure 10-figure supplement 3

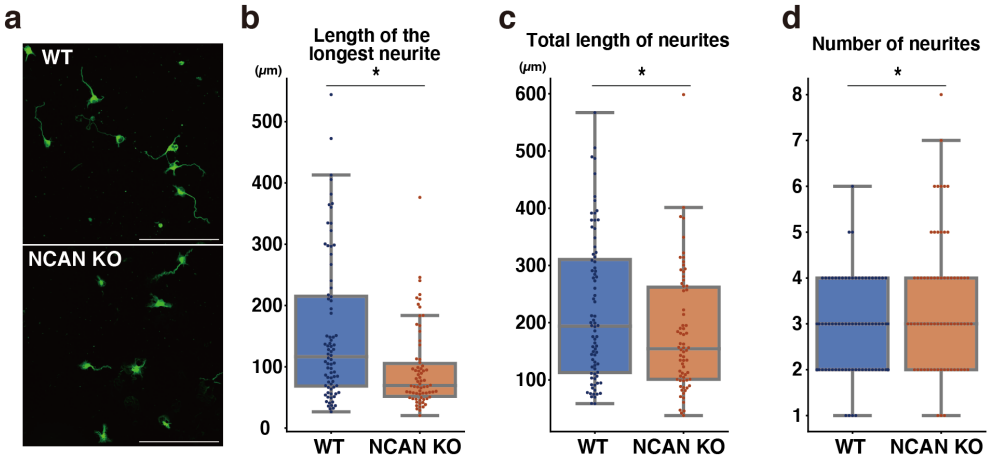

1052

1053 **Figure 10-figure supplement 3.** Neurite outgrowth analysis of WT and NCAN KO neurons with anti-Tuj-
1054 1 antibody staining (**a**) Representative images of WT and NCAN KO neurons stained with anti-Tuj-1
1055 antibody after 3 days of culture. (**b-d**) The length of the longest neurite (b), total length of neurites (c), and
1056 number of neurites (d) of neurons. Neurites were analyzed using AutoNeuriteJ. N = 70–80 cells per
1057 condition. *$p < 0.05$; Student's t-test.

1058

1059 **Key resources table**

REAGENT or RESOURCE	SOURCE	IDENTIFIER
Antibodies		
Anti-tenascin C Rat IgG2A (Clone # 578) Anti Tenascin	R&D	MAB2138
Anti-β-Tubulin (Tuj-1) Mouse IgG1(clone TUB 2.1)	Sigma	T4026
Anti-Neurocan Sheep IgG	R&D	AF5800
Anti-GFP Alexa Fluor 488 conjugate Rabbit IgG	Invitrogen	A21311
Anti-Nestin Mouse IgG	Millipore	2780475
Anti-Pax6 Rabbit IgG	Invitrogen	015-27293
Anti-EOMES (Tbr2) Rat IgG2A	Invitrogen	14-4875-82
Anti-NeuN Rabbit IgG	Proteintech	26975-1-AP
Anti-GAPDH Mouse IgG1(Clone # 5A12)	Wako	016-25523
Anti-Chondroitine-4-Sulfate Mouse IgG1 (Clone # BE-123)	Millipore	2574085
Alexa Fluor 488 donkey anti-Mouse (H+L)	Wako	715-545-151
Alexa Fluor 594 goat anti-Rat IgG (H+L)	Thermo Fisher	A-11007
Alexa Fluor 647 goat anti-Rat IgG (H+L)	Thermo Fisher	A-21247
Alexa Fluor 647 donkey anti-Sheep IgG (H+L)	Thermo Fisher	A-21448
Mouse IgG HRP-conjugated Antibody	MBL	PM009-7
Sheep IgG HRP-conjugated Antibody	R&D	HAF016
Rat IgG HRP-conjugated Antibody	Cell Signaling Technology	7077S
Rabbit IgG HRP-conjugated Antibody	Cell Signaling Technology	7074S
Bacterial and virus strains		
Biological samples		
Chemicals, peptides, and recombinant proteins		
Alt-R S.p. Cas9 Nuclease V3	IDT	Catalog #1081058
Trypsin (Sequencing Grade)	Promega	V511C
HRP-conjugated streptavidin	Wako	190-17441
GFP-Trap-Agarose	Chromotek	gta-20
DAPI solution	DOJINDO	Lot.PF082 340-07971
N-2 Supplement	Thermo Fisher	17502-048
B-27 Supplement	Thermo Fisher	17504-044
Neurobasal Medium	Thermo Fisher	21103-049
Penicillin-Streptomycin	Thermo Fisher	15070-063
HBSS (X10)	Thermo Fisher	14185-052

HEPES (1M)	Thermo Fisher	15630-080
Papain	Worthington Biochemical Corporation	LK003178
Fast Green	Wako	061-00031
Protease Inhibitor Cocktail	Sigma	P8340-1ML
Streptavidin Magnetic Beads	Thermo Fisher	88817
Poly-L-Ornithine Solution	Wako	163-27421
Skim Milk Powder	Wako	190-12865
Immobilon Transfer Membrane PVDF	Millipore	IPVH00010
Immobilon Western Chemiluminescent	Millipore	WBKLS0500
Hyaluronidase from streptomyces hyalurolyticus	Sigma	H1136
Recombinant Human Tenascin C Protein	R&D	3358-TC
Recombinant Human Neurocan Protein	R&D	6508-NC-050
Chondroitinase ABC Protease Free	Seikagaku Corporation	100332
Sodium Hyaluronate (M2) (Mw:600,000~1,120,000)	PG Research	NaHA-M2
Biotinylated Sodium Hyaluronate (M1) (Mw:600,000~1,120,000)	PG Research	BHHA-M1
Carboxyfluorescein diacetate succinimidyl ester	DOJINDO	341-07401
ELISA 96 well plate	IWAKI	3801-096
BLOCK ACE Powder	KAC	UKB80
ELISA POD Substrate TMB Solution	Nacalai	05299-54
Hyaluronan Binding Protein (HABP)	Cosmo-bio	BC40
Hyaluronic Acid Sodium Salt	Wako	083-10341
Streptavidin, Alexa Fluor 488 conjugate	Thermo Fisher	S-11223
Biotinylated Hyaluronan Binding Protein	Hokudo	BC41
SuperScript III reverse transcriptase	Thermo Fisher	18080044
OCT Compound	Sakura Finetek	45833
Anion exchange chromatography resin	Tosoh	TOYOPEARL DEAE-650M
Heparin-agarose	Sigma	H6508
Ultrafiltration filter	Amicon	YM-10
α-cyano-4-hydroxycinnamic acid	Shimadzu	70990
Lipofectamine 3000 Reagent	Thermo Fisher	L3000008
Critical commercial assays		
BCA assay kit	Thermo Fisher	23227

RNeasy Mini Kit	Qiagen	74104
PowerUp SYBR Green Master Mix	Thermo Fisher	A25741
DIG RNA Labeling Kit (SP6/T7)	Roche	11175025910
NEBuilder HiFi DNA Assembly Master Mix	New England Biolabs	E2621
In-Fusion HD Cloning Kit	Takara	639648
KOD -Plus- Mutagenesis Kit	Toyobo	SMK-101
Deposited data		
Experimental models: Cell lines		
HEK293	Riken Cell Bank	RCB1637
HEK293T	Riken Cell Bank	RCB2202
Experimental models: Organisms/strains		
ICR mice	Japan SLC	RRID: MGI:5462094
C57BL/6N mice	Japan SLC	RRID: MGI:5295404
B6.Cg-Tnc<tm1Sia>/Rbrc	RIKEN Bioresource Center	RBRC00169
DKO mice for TNC and NCAN	This paper	N/A
Oligonucleotides		
ISH TNC probe f: CGGAATTCATCTTTGCAGAGAAAGGACAGC	This paper	N/A
ISH TNC probe r: GCTCTAGACTGTGTCCTTGTCATAGGTGGA	This paper	N/A
ISH NCAN probe f: GCGAATTCAGAATGCCTCTCTTGTTGGTG	This paper	N/A
ISH NCAN probe r: GCTCTAGACTACAATAGTGAGTTCGAGGCC	This paper	N/A
crRNA, Mm.Cas9.NCAN.1.AA: ACCUUAGUCCACUUGAUCCGGUUUUAGAGCUAUGCU	IDT	REF #101658344
Alt-R CRISPR-Cas9 tracrRNA	IDT	#1072533
qPCR for Ncan: forward, 5'-CCCTGCTTCTTTACCCTGCA-3'; reverse, 5'-CGTTGTCTTTGGCCACCAAG-3'	This paper	N/A
qPCR for Tnc: forward, 5'-ACCATGGGTACAGGCTGTTG-3'; reverse, 5'-CCTTTCCAGCCTGGTTCACA-3'	This paper	N/A

qPCR for Gapdh: forward, 5'-GACTTCAACAGCAACTCCCAC-3'; reverse, 5'-TCCACCACCCTGTTGCTGTA-3'	This paper	N/A
Recombinant DNA		
pCAG-GFP	Addgene	Plasmid #11150
pCAG-mGFP	Addgene	Plasmid #14757
pCAG-mCherry	This paper	N/A
pCAGGS-TurboRFP	This paper	N/A
pCAG-Full length NCAN-GFP	This paper	N/A
pCAG-N half NCAN-GFP	This paper	N/A
pCAG-C half NCAN-GFP	This paper	N/A
Software and algorithms		
MASCOT server	Matrix science	https://www.matrixscience.com/server.html
ImageJ	Schneider et al., 2012	https://imagej.nih.gov/ij/
Other		
Electroporator	NEPA GENE	NEPA21
5 mm-diameter tweezers-type disc electrodes	NEPA GENE	CUY650P5
2.5 mm x 4mm tweezers-type disc electrodes	NEPA GENE	CUY652P2.5X4
Vibratome	Leica	VT1200S
LuminoGraph	ATTO	WSE-6100H-ACP
Confocal laser scanning microscope	Nikon	AX
Confocal laser scanning microscope	Carl Zeiss	LSM 710 NLO
Fluorescence stereomicroscope	Leica	M165FC
Animal anesthetizer	Muromachi	MK-AT210
StepOne Real-Time PCR System	Thermo Fisher	4376374
Cryostat	Leica	CM3050 S
Direct nanoLC/MALDI fraction system	KYA technologies	DiNa-MaP
MALDI mass spectrometer	SCIEX	TOF/TOF 5800
LC-MS/MS System	SCIEX	QTRAP 5500
Fluorescence-activated cell sorter	Bay bioscience	JSAN

1060